# Production of K∗(892)0 and ϕ(1020) in pp and Pb-Pb collisions at √sNN = 5.02 TeV

**(ALICE Collaboration) Acharya, S.; ...; Erhardt, Filip; ...; Gotovac, Sven; ...; Jerčić, Marko; ...; Karatović, David; ...; ...**

*Source / Izvornik:* **Physical Review C, 2022, 106**

**Journal article, Published version**
**Rad u časopisu, Objavljena verzija rada (izdavačev PDF)**

https://doi.org/10.1103/PhysRevC.106.034907

*Permanent link / Trajna poveznica:* https://urn.nsk.hr/urn:nbn:hr:217:425973

# Production of $K^*(892)^0$ and $\phi(1020)$ in $pp$ and Pb-Pb collisions at $\sqrt{s_{NN}} = 5.02$ TeV

S. Acharya *et al.*[*]
(ALICE Collaboration)

(Received 10 July 2021; accepted 19 August 2022; published 14 September 2022)

The production of $K^*(892)^0$ and $\phi(1020)$ mesons in proton–proton ($pp$) and lead–lead (Pb–Pb) collisions at $\sqrt{s_{NN}} = 5.02$ TeV has been measured using the ALICE detector at the Large Hadron Collider (LHC). The transverse momentum ($p_T$) distributions of $K^*(892)^0$ and $\phi(1020)$ mesons have been measured at midrapidity ($|y| < 0.5$) up to $p_T = 20$ GeV/$c$ in inelastic $pp$ collisions and for several Pb–Pb collision centralities. The collision centrality and collision energy dependence of the average transverse momenta agree with the radial flow scenario observed with stable hadrons, showing that the effect is stronger for more central collisions and higher collision energies. The $K^{*0}/K$ ratio is found to be suppressed in Pb–Pb collisions relative to $pp$ collisions: this indicates a loss of the measured $K^*(892)^0$ signal due to rescattering of its decay products in the hadronic phase. In contrast, for the longer-lived $\phi(1020)$ mesons, no such suppression is observed. The nuclear modification factors ($R_{AA}$) of $K^*(892)^0$ and $\phi(1020)$ mesons are calculated using $pp$ reference spectra at the same collision energy. In central Pb–Pb collisions for $p_T > 8$ GeV/$c$, the $R_{AA}$ values of $K^*(892)^0$ and $\phi(1020)$ are below unity and observed to be similar to those of pions, kaons, and (anti)protons. The $R_{AA}$ values at high $p_T$ (>8 GeV/$c$) for $K^*(892)^0$ and $\phi(1020)$ mesons are in agreement within uncertainties for $\sqrt{s_{NN}} = 5.02$ and 2.76 TeV.

DOI: 10.1103/PhysRevC.106.034907

## I. INTRODUCTION

Experiments at the Large Hadron Collider (LHC) at CERN have recorded Pb–Pb collisions at the center of mass energy $\sqrt{s_{NN}} = 5.02$ TeV, to date the highest energy for collisions of heavy ions, that has allowed for the creation of a long-lived, hot, dense, and strongly interacting QCD matter [1,2]. One of the physics interests of ALICE experiment is to study the properties of the deconfined state of quarks and gluons (the quark-gluon plasma, QGP) produced in the early stages of the collision relative to the confined state of hadrons and resonances (excited state hadrons) [3–5]. In these collisions, several kinds of hadrons and resonances with different flavors of valence quark content, mass, spin, and lifetime are produced. Each of these hadrons and resonances possesses unique characteristic features that can be exploited to study the properties of the medium [6]. Strongly decaying resonances like $K^*(892)^0$ and $\phi(1020)$ with strange valence quarks have similar masses and spin = 1, but different lifetimes of $4.16 \pm 0.05$ fm/$c$ and $46.3 \pm 0.4$ fm/$c$ [7], respectively. The large difference in the lifetimes of these resonances allows one to probe the system formed in heavy-ion collisions at different timescales [8–22].

Experiments usually measure the transverse momentum ($p_T$), rapidity ($y$), and azimuthal angle ($\varphi$) distributions of the produced particles. Other observables are mostly derived from these basic measurements. The total yields of the resonances like $K^*(892)^0$ and $\phi(1020)$ dominantly come from the low transverse momentum ($p_T < 3$ GeV/$c$) particles and are sensitive to the rescattering and regeneration processes in the hadronic phase of the heavy-ion collisions [10,14,18,20,21]. Further, the $p_T$-integrated yields have been used to construct various particle ratios to understand strangeness enhancement in high-energy collisions [10,12–14,18,19,21,23]. In the intermediate $p_T$ range (3–6 GeV/$c$), effects of radial flow and recombination have been probed [24,25]. Different kinds of particle ratios, particularly baryon-to-meson, have been used to understand these dynamics [18,19,21,26–29]. At high $p_T$, the phenomenon of energy loss by energetic partons traversing the dense medium formed in high-energy heavy-ion collisions has been studied [27,30–38]. The energy loss process depends on the initial medium density, on the lifetime of the dense matter, on the path length traversed by the parton, and on the quark flavor. The contributions of these parameters can be understood by studying the identified hadron $p_T$ spectra for various collision centralities and collision energies relative to $pp$ collisions.

ALICE has previously measured the $K^*(892)^0$ and $\phi(1020)$ meson production in $pp$ and Pb–Pb collisions at $\sqrt{s_{NN}} = 2.76$ TeV [18,21]. The low-$p_T$ physics phenomena of rescattering of resonance decay products and regeneration of resonances in hadronic medium, radial flow, and strangeness enhancement are addressed through the measurements of the particle yield ($dN/dy$), yield ratios, and mean transverse momentum ($\langle p_T \rangle$). The measured $\langle p_T \rangle$ in central

[*]Full author list given at the end of the article.



 

Pb–Pb collisions is observed to be 15–20% higher than in peripheral collisions and is also higher than the $\langle p_{\mathrm{T}} \rangle$ measured in nucleus–nucleus collisions at RHIC energies [10,12–14], suggesting a stronger radial flow effect at the LHC. In Ref. [27], it is shown that $\langle p_{\mathrm{T}} \rangle$ of $\pi$, $K$, and $p$ in central Pb–Pb collisions is slightly higher at 5.02 TeV than at 2.76 TeV. This effect is consistent with the presence of a stronger radial flow at the highest collision energy in Pb–Pb collisions. The $K^*(892)^0$ and $\phi(1020)$ resonances, having a mass similar to the mass of the proton, can further be used to test this effect. The $p_{\mathrm{T}}$-integrated yield of $K^*(892)^0$ relative to kaons is observed to be suppressed in central Pb–Pb collisions compared to $pp$ and peripheral Pb–Pb collisions. No such suppression is observed for the $\phi(1020)$ meson. This suggests that the rescattering of the decay products of the short-lived resonance $K^*(892)^0$ in the hadronic phase is the mechanism that determines the reduced measurable yield. This characteristic is further supported by the expectations from thermal model predictions for Pb–Pb collisions with a chemical freezeout temperature of 156 MeV, which does not include rescattering effect [39]. A detailed study on the energy and system size dependence of $p_{\mathrm{T}}$-integrated particle yield ratios, $K^{*0}/K$ and $\phi/K$ is performed. For current measurements, these ratios are calculated with the average of particle and anti-particle yields i.e. $(K^{*0} + \overline{K}^{*0})/(K^+ + K^-)$ and $2\phi/(K^+ + K^-)$, which are denoted as $K^{*0}/K$ and $\phi/K$, respectively throughout this paper unless specified otherwise. The reader is referred to Ref. [22] for more elaborate discussions on the observation of rescattering in Pb–Pb collisions, lifetime of the hadronic phase and physics related to $p_{\mathrm{T}}$ dependence of particle ratios involving $K^*(892)^0$ and $\phi(1020)$ resonances in Pb–Pb collisions at $\sqrt{s_{NN}} = 5.02$ TeV.

The comparison of $K^*(892)^0$ and $\phi(1020)$ $p_{\mathrm{T}}$ distributions to the expected $p_{\mathrm{T}}$ distributions from a blast-wave function [40] with parameters obtained from combined fits to $\pi^{\pm}$, $K^{\pm}$, and $p(\bar{p})$ [41], which does not include rescattering effects, shows a suppression of the $K^*(892)^0$ yield by $\approx$40% for $p_{\mathrm{T}} < 3$ GeV/$c$. However, it is not yet established if the observed $p_{\mathrm{T}}$-dependence of the $K^*(892)^0$ suppression is only due to the rescattering effect. No such suppression is observed for the $\phi(1020)$ meson, suggesting that $\phi(1020)$ mesons typically decay outside the fireball (lifetime $\approx$10 fm/$c$ [42]) because of their longer lifetime.

The high-$p_{\mathrm{T}}$ parton energy loss is studied by measuring the nuclear modification factor ($R_{AA}$). It is defined as

$$R_{AA} = \frac{1}{\langle T_{AA} \rangle} \frac{d^2N^{AA}/(dy dp_{\mathrm{T}})}{d^2\sigma^{pp}/(dy dp_{\mathrm{T}})}, \tag{1}$$

where $d^2N^{AA}/(dy dp_{\mathrm{T}})$ is the yield of particles in heavy-ion collisions and $\sigma^{pp}$ is the production cross section in $pp$ collisions. $\langle T_{AA} \rangle = \langle N_{\mathrm{coll}} \rangle / \sigma_{\mathrm{inel}}$ is the average nuclear overlap function, where $\langle N_{\mathrm{coll}} \rangle$ is the average number of binary nucleon–nucleon collisions calculated using MC Glauber [43] simulations, and $\sigma_{\mathrm{inel}}$ is the inelastic $pp$ cross section equal to $(67.6 \pm 0.6)$ mb at $\sqrt{s_{NN}} = 5.02$ TeV [27,44]. The $R_{AA}$ measurements in Pb–Pb collisions at $\sqrt{s_{NN}} = 2.76$ TeV [10,31] show that at high transverse momentum ($p_{\mathrm{T}} > 8$ GeV/$c$) nuclear modification factors for $\pi$, $K$, $p$, $K^*(892)^0$, and $\phi(1020)$ are consistent within uncertainties. This suggests that the partonic energy loss in the dense medium produced in heavy-ion collisions does not change the relative particle abundancies at $p_{\mathrm{T}} > 8$ GeV/$c$ in the light quark sector ($u, d, s$). The new measurements in $pp$ and Pb–Pb collisions at $\sqrt{s_{NN}} = 5.02$ TeV will be useful in the study of energy dependence of $R_{AA}$ and in further testing the flavor dependence of partonic energy loss in the dense medium produced in heavy-ion collisions. The centrality, collision energy and flavor dependence of the $R_{AA}$ are studied using precise measurements at the highest beam energy available for Pb–Pb collisions at the LHC.

In this article, $K^*(892)^0$ and $\phi(1020)$ meson production is studied at midrapidity, $|y| < 0.5$, over a wide transverse momentum range up to 20 GeV/$c$ in Pb–Pb and inelastic $pp$ collisions at $\sqrt{s_{NN}} = 5.02$ TeV. Throughout this article, the results for $K^*(892)^0$ and $\overline{K}^*(892)^0$ are averaged and denoted by the symbol $K^{*0}$, and $\phi(1020)$ is denoted by $\phi$ unless specified otherwise. The article is organized as follows: Section II describes the data analysis techniques, which include the event and track selection, the technique adopted to obtain the yields of the resonances, correction factors and systematic uncertainties. Section III presents results related to the $K^{*0}$ and $\phi$ meson $p_{\mathrm{T}}$ spectra, yields, mean transverse momentum, particle ratios and nuclear modification factors. A summary of the work presented in the article is given in Sec. IV.

## II. DATA ANALYSIS

The measurements of $K^{*0}$ and $\phi$ meson production in $pp$ and Pb–Pb collisions at $\sqrt{s_{NN}} = 5.02$ TeV have been performed on data taken with the ALICE detector in the year 2015. The resonances are reconstructed via their hadronic decay channels, $K^{*0} \rightarrow \pi^{\pm}K^{\mp}$ (B.R. = 66.6% [7]) and $\phi \rightarrow K^+K^-$ (B.R. = 49.2% [7]). In $pp$ collisions, $K^{*0}$ and $\phi$ mesons are measured in inclusive inelastic events, whereas in Pb–Pb collisions they are measured in eight collision centrality classes 0–10%, 10–20%, 20–30%, 30–40%, 40–50%, 50–60%, 60–70%, and 70–80% [45].

### A. Event and track selection

A detailed description of the ALICE detector can be found in Refs. [46,47]. The measurements are obtained with the ALICE central barrel detectors, which are located inside a solenoidal magnet providing a magnetic field of 0.5 T, and are used for tracking, particle identification and reconstruction of the primary vertex. The measurements have been performed by using central barrel detectors: the inner tracking system (ITS), the time projection chamber (TPC), and the time-of-flight (TOF) detector. These detectors have full azimuthal coverage around midrapidity, at pseudorapidity $|\eta| < 0.9$. The primary vertex position is determined from global tracks [47]. Global tracks are reconstructed using both the TPC and ITS, and are used to determine the primary vertex position [47]. Events are selected according to the position of the primary vertex along the beam axis ($v_z$), which is required to be within 10 cm from the nominal interaction point to ensure a uniform acceptance and reconstruction efficiency in the pseudorapidity region $|\eta| < 0.8$. In addition, the difference between the

vertices reconstructed with the two innermost layers of the ITS and those reconstructed with global tracks ($|v_{z,\text{Track}} - v_{z,\text{SPD}}|$) is required to be less than 0.5 cm. This selection is required to reject pile-up events in $pp$ collisions, which are less than 1% of the overall number of events. Pb–Pb collisions have negligible pile-up. A pair of scintillator arrays (V0 detector) that cover the pseudorapidity region $2.8 < \eta < 5.1$ (V0-A) and $-3.7 < \eta < -1.7$ (V0-C), is used for the interaction trigger both in $pp$ and in Pb–Pb collisions. The trigger is defined as a coincidence between the V0-A and the V0-C. In addition, at least one hit in the central barrel detector SPD is required for the minimum bias trigger in $pp$ collisions. The V0 detector signal is the total charge collected (V0M amplitude) in the detector, which is proportional to the charged particle multiplicity in its acceptance, and it is used to classify the Pb–Pb events into centrality classes, defined in terms of percentiles of the hadronic cross section. A Glauber Monte Carlo model is fitted to the V0 amplitude distribution to compute the fraction of the hadronic cross section corresponding to any given range of V0 amplitudes. Based on these studies, the data are divided into several centrality classes [48]. The number of events analyzed after the event selections are $\approx 110 \times 10^6$ and $\approx 24 \times 10^6$ in minimum bias $pp$ and Pb–Pb collisions, respectively.

$K^{*0}$ and $\phi$ mesons are reconstructed using global tracks. To ensure high tracking efficiency and to limit the contamination due to secondary particles and tracks with wrongly associated hits, global selected tracks are required to have a minimum number of TPC hits associated to the track (70 of a maximum of 159). The reconstructed track $\chi^2$ normalized to the number of TPC clusters is required to be lower than 4. To reduce the contamination from beam-background events and secondary particles coming from weak decays, selection criteria on the distance of closest approach to the primary vertex in the transverse plane ($\text{DCA}_{xy}$) of the selected tracks and in the beam direction ($\text{DCA}_z$) are applied [47]. The value of $\text{DCA}_{xy}$ is required to be $\text{DCA}_{xy}\ (p_\text{T}) < 0.0105 + 0.035 p_\text{T}^{-1.1}$ cm ($p_\text{T}$ in GeV/$c$) which corresponds to 7 times the $\text{DCA}_{xy}$ resolution, and $\text{DCA}_z$ is required to be less than 2 cm. The $p_\text{T}$ is requested to be larger than 0.15 GeV/$c$. The charged tracks are selected within the pseudorapidity range $|\eta| < 0.8$, which ensures uniform acceptance and the best reconstruction efficiency. Furthermore, the charged tracks from the decay of weakly decaying kaons are rejected.

The TPC and TOF are used to identify pions and kaons by measuring the specific ionization energy loss ($dE/dx$) in the TPC and their time-of-flight in the TOF, respectively. Whenever the TOF information for a given track is not available, only the TPC information is used for particle identification. The $dE/dx$ resolution of the TPC is denoted as $\sigma_\text{TPC}$. For $K^{*0}$ and $\phi$ meson reconstruction in Pb–Pb collisions, and $K^{*0}$ reconstruction in $pp$ collisions, pion and kaon candidates are required to have $\langle dE/dx \rangle$ within $2\sigma_\text{TPC}$ of the expected $dE/dx$ values for each particle species over the whole momentum range. To further reduce the number of misidentified particles, the measured time-of-flight is required not to deviate from the expected value for each given mass hypothesis by more than $3\sigma_\text{TOF}$ ($\sigma_\text{TOF} \approx 60$ ps) [27]. For $\phi$ meson reconstruction in $pp$ collisions, the kaon candidates are selected using the TPC with selection criteria of $6\sigma_\text{TPC}$, $4\sigma_\text{TPC}$, and $2\sigma_\text{TPC}$ on the measured $\langle dE/dx \rangle$ distributions in the momentum ranges $p < 0.3$ GeV/$c$, $0.3 < p < 0.4$ GeV/$c$, and $p > 0.4$ GeV/$c$, respectively. In addition, a $3\sigma_\text{TOF}$ selection criterion is applied on the time-of-flight over the measured momentum range whenever the TOF information is available.

### B. Yield extraction

The raw yields are extracted in each $p_\text{T}$ bin and centrality class as done in previous work [18,21,49–51]. The $p_\text{T}$ spectra for $K^{*0}$ ($\phi$) mesons cover the range 0–20 GeV/$c$ (0.4–20 GeV/$c$) for $pp$ collisions. For Pb–Pb collisions, the $p_\text{T}$ spectra of $K^{*0}$ and $\phi$ mesons are measured from $p_\text{T} = 0.4$ GeV/$c$ up to 20 GeV/$c$ in all centrality classes. The $K^{*0}$ and $\phi$ mesons are reconstructed via their hadronic decay channels by calculating the invariant mass of their decay daughters. For each event, the unlike-sign kaons and pions are paired for $K^{*0}$, and unlike-sign kaons are paired for the $\phi$ meson to construct the invariant-mass distribution. The rapidity of the daughters pair is required to lie in the range, $|y| < 0.5$. An event mixing technique is used to estimate the combinatorial background where the kaons and pions from one event are mixed with oppositely charged kaons and pions from other events. Two events are mixed only if they have similar multiplicity ($|\Delta n| < 5$) and collision vertex ($|\Delta v_z| < 1$ cm). To reduce the statistical uncertainties from the background distribution, each event is mixed with five other events. Then the mixed-event invariant mass distribution is normalized in the mass region outside of the mass peak, namely $1.1 < M_{K\pi} < 1.15$ GeV/$c^2$ and $1.035 < M_{KK} < 1.045$ GeV/$c^2$ for $K^{*0}$ and $\phi$ mesons, respectively. The left panels of Figs. 1 and 2 show the invariant mass distributions of unlike-sign $K\pi$ and $KK$ pairs from the same event (black marker) and the normalized mixed event background (red marker) for the transverse momentum ranges $1.2 < p_\text{T} < 1.6$ GeV/$c$ and $0.8 < p_\text{T} < 1.0$ GeV/$c$, respectively. The invariant mass distributions are shown for the 0–10% and 70–80% centrality classes in Pb–Pb collisions. The combinatorial background subtracted invariant-mass distributions are fitted using a combined function to describe the signal peak and the residual background. As shown in the right panels of Figs. 1 and 2, respectively, a Breit-Wigner function [Eq. (2)] is used to describe the $K^{*0}$ peak and a Voigtian function [a convolution of a Breit-Wigner and a Gaussian function, Eq. (3)] is used to describe the $\phi$ peak. A second order polynomial is used to describe the residual background in both cases. The residual background is what remains after the combinatorial background subtraction and it is mainly due to correlated pairs from real resonance decays where the daughter particles are misidentified as $K$ or $\pi$. The signal peak fit functions for $K^{*0}$ and $\phi$ are

$$\frac{dN}{dM_{K\pi}} = \frac{N_\text{raw}}{2\pi} \frac{\Gamma}{(M_{K\pi} - M_0)^2 + \frac{\Gamma^2}{4}}, \tag{2}$$

$$\frac{dN}{dM_{KK}} = \frac{N_\text{raw}}{2\pi} \int \frac{\Gamma}{(M_{KK} - m')^2 + \Gamma^2/4} \frac{e^{-(m'-M_0)^2/2\sigma^2}}{\sqrt{2\pi}\sigma} dm', \tag{3}$$

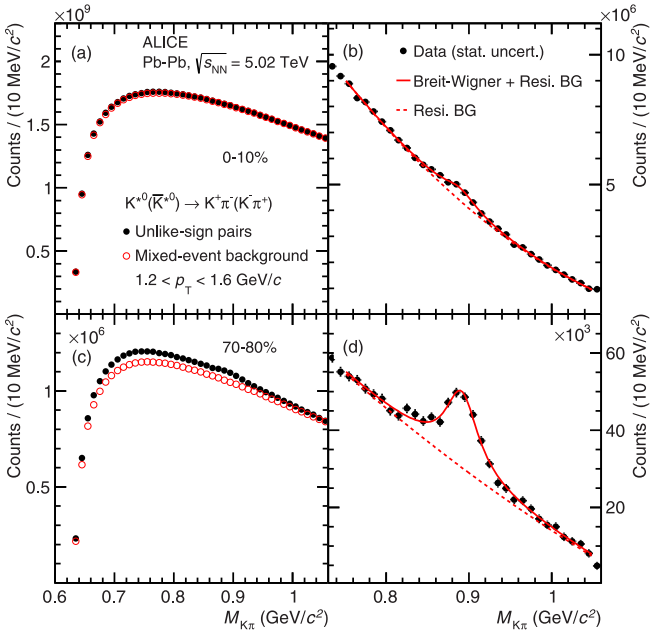


FIG. 1. Invariant-mass distributions of $\pi K$ pairs for the 0–10% and 70–80% centrality classes in Pb–Pb collisions at $\sqrt{s_{NN}} = 5.02$ TeV for the transverse momentum range $1.2 < p_T < 1.6$ GeV/$c$. The left panels show the unlike charge $\pi K$ invariant-mass distribution from the same event and the normalized mixed event background. The right panels report the invariant-mass distribution after subtraction of the combinatorial background for $K^{*0}$. The solid curves represent fits to the distributions and the dashed curves are the components of the fits that describe the residual background. The statistical uncertainties are shown by bars.

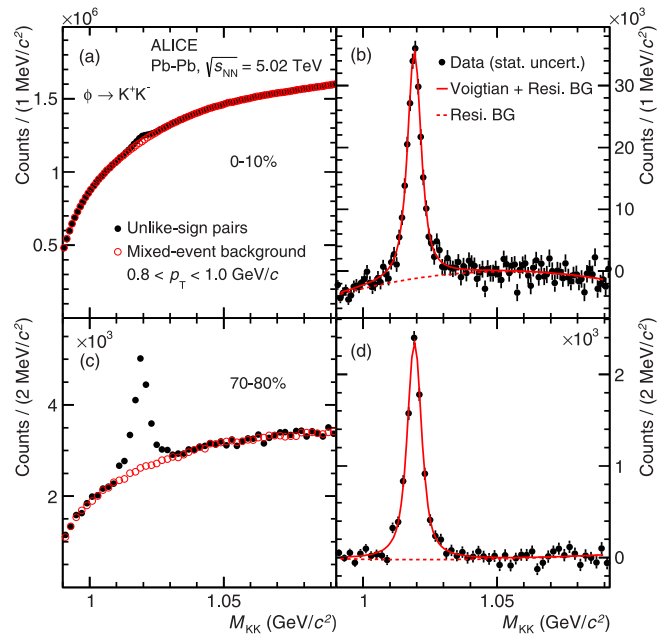


FIG. 2. Invariant-mass distributions of $KK$ pairs for the 0–10% and 70–80% centrality classes in Pb–Pb collisions at $\sqrt{s_{NN}} = 5.02$ TeV for the transverse momentum ranges $0.8 < p_T < 1.0$ GeV/$c$. The left panels show the unlike charge $KK$ invariant-mass distribution from the same event and the normalized mixed event background. The right panels report the invariant-mass distribution after subtraction of the combinatorial background for $\phi$. The solid curves represent fits to the distributions and the dashed curves are the components of the fits that describe the residual background. The statistical uncertainties are shown by bars.

where $M_{K\pi}$ and $M_{KK}$ are the reconstructed invariant masses of $K^{*0}$ and $\phi$ mesons. $M_0$, $\Gamma$, and $N_{\rm raw}$ are the mass, width and raw yield of the resonances, respectively. The parameter $\sigma$ in Eq. (3) represents the mass resolution, which depends on $p_T$. The widths of $K^{*0}$ and $\phi$ are fixed to the vacuum values [7] while fitting the invariant mass distributions. For the $\phi$ meson, the $\sigma$ is kept free. The measured $\sigma$ on the $\phi$ mass is $p_T$ dependent, varies between 1–2 MeV/$c^2$ and its values are consistent with the values obtained from Monte Carlo simulations. The raw particle yields are extracted by integrating the invariant mass distribution within the mass interval approximately $M_0 \pm 2\Gamma$ and subtracting the integral of the residual background function in the same mass region. The resonance yields beyond the integration region are obtained by integrating the tail part of the signal fit function; these yields are then added to the yields extracted by integrating the invariant mass distribution.

### C. Yield correction

#### *1. Acceptance and reconstruction efficiency*

The raw transverse momentum distributions are corrected for the detector acceptance and reconstruction efficiency ($A \times \epsilon_{\rm rec}$). These correction factors are evaluated by using Monte Carlo (MC) events generated with PYTHIA8 (Monash 2013 Tune) [52] for $pp$ and HIJING [53] for Pb–Pb collisions, and by transporting the particles through a full simulation of the ALICE detector with GEANT3 [54]. The $A \times \epsilon_{\rm rec}$ has a centrality dependence in Pb–Pb collisions and a deviation of ≈5–7% is observed from the most central to the most peripheral centrality classes. As the real data and the generated MC spectral shapes are different, the $p_T$ spectra of the generated mesons are reweighted to the respective $p_T$ spectra from the data in an iterative method to re-estimate the efficiency [55]. The effect of re-weighting the generated $p_T$ spectra on $A \times \epsilon_{\rm rec}$ is ∼4–6% at low-$p_T$ (<1 GeV/$c$) and is negligible at high $p_T$ (>1 GeV/$c$).

#### *2. Normalization*

The normalized yield is given by

$$\frac{1}{N_{\rm event}} \frac{d^2N}{dy dp_T} = \frac{1}{N^{\rm acc}_{\rm event}} \frac{N_{\rm raw}}{\Delta y \Delta p_T} \frac{\epsilon_{\rm trig}\, \epsilon_{\rm vert}\, \epsilon_{\rm SL}}{(A \times \epsilon_{\rm rec})\, BR}, \quad (4)$$

where $\Delta y$ and $\Delta p_T$ are the widths of rapidity and $p_T$ bins, respectively. The raw spectra are corrected for the branching ratio (BR). The extracted yields are normalized to the number of analyzed events ($N^{\rm acc}_{\rm event}$). In order to obtain the absolute resonance yields per inelastic $pp$ collision, the factor $\epsilon_{\rm trig} = 0.757 \pm 0.019$ due to trigger efficiency is used. This is the ratio between the V0 visible cross section [56] and the inelastic cross section [44].

The correction factor $\epsilon_{\rm vert}$ accounts for the vertex reconstruction efficiency, which is calculated as the ratio of the number of events having good vertex to the total number of triggered events. This is estimated to be 0.958 in $pp$ collisions. The signal loss correction, $\epsilon_{\rm SL}$ accounts for the loss in $K^{*0}$ and $\phi$ yields that is caused by the event selection with minimum bias trigger, rather than all inelastic events. The $\epsilon_{\rm SL}$ has a $p_{\rm T}$ dependence and is only significant for low $p_{\rm T}$ (<2.5 GeV/$c$). It is calculated as the ratio of the $p_{\rm T}$ spectrum from inelastic events to the $p_{\rm T}$ spectrum from triggered events. The value of $\epsilon_{\rm SL}$ is less than 1.05 for both $K^{*0}$ and $\phi$ mesons in $pp$ collisions. The effects of inelastic trigger, vertex reconstruction efficiency and signal loss corrections are negligible in Pb–Pb collisions [28,41] and, hence, are not considered.

### D. Systematic uncertainties

The systematic uncertainties in the measurement of $K^{*0}$ and $\phi$ production in $pp$ and Pb–Pb collisions at $\sqrt{s_{NN}}$ = 5.02 TeV have been estimated by considering uncertainties due to signal extraction, track selection criteria, particle identification, global tracking efficiency, uncertainty in the material budget of the ALICE apparatus and the hadronic interaction cross section in the detector material. To study the systematic uncertainty for $K^{*0}$ and $\phi$ in Pb–Pb and $K^{*0}$ in $pp$, an approach similar to that described in Refs. [18,21,49,51] has been adopted. For the estimation of systematic uncertainties for $\phi$ in $pp$, a similar approach is followed as in Refs. [57,58].

A summary of the systematic uncertainties from various sources, for $K^{*0}$ and $\phi$ in $pp$ and Pb–Pb collisions is given in Ref. [22] where the values of relative systematic uncertainties are quoted for low, intermediate, and high $p_{\rm T}$. The track selection criteria have been varied to study the systematic effect due to the track selection. In order to study the effect of the choice of particle identification criteria of the daughter tracks on raw yield extraction, the selection criteria on TPC and TOF have been varied. To estimate the systematic uncertainty of particle identification (PID), the $N\sigma_{\rm TPC/TOF}$ cut is varied by $1\sigma_{\rm TPC/TOF}$ from the default PID selection criterion.

The uncertainty due to the signal extraction includes variations of the event mixing background normalization range, signal fit range, residual background fit function, choice of combinatorial background, and mass resolution. The mixed event background distributions for $K^{*0}$ and $\phi$ have been normalized in different invariant-mass regions excluding the signal peaks; the change in yield is considered as the systematic uncertainty. The $K\pi$ invariant-mass fitting ranges are varied by 10–50 MeV/$c^2$ for $K^{*0}$ whereas for the $\phi$ the $KK$ invariant-mass fitting ranges are varied by 5–10 MeV/$c^2$. The residual background is fitted with a third-order polynomial for Pb–Pb collisions, and in $pp$ collisions, a first- and third-order polynomial is used for systematic studies. The systematic uncertainties due to the combinatorial background are estimated by changing the method of background reconstruction (like sign and event mixing).

Another source of uncertainty comes from the determination of the global tracking efficiency, which arises from the ITS-TPC track matching efficiency. The systematic uncertainties due to global tracking efficiency are calculated from the corresponding values for single charged particles uncertainty and by combining the two charged tracks used in the invariant mass reconstruction of $K^{*0}$ and $\phi$. In both $pp$ and Pb–Pb collisions, this contribution has been estimated to be $p_{\rm T}$ dependent for charged particles [28].

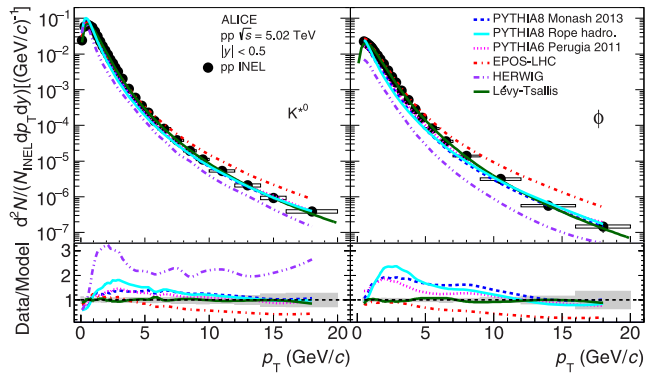


FIG. 3. Transverse momentum spectra of $K^{*0}$ (left panel) and $\phi$ (right panel) for inelastic $pp$ collisions at $\sqrt{s}$ = 5.02 TeV. The statistical and systematic uncertainties are shown by bars and boxes, respectively. The results are compared with model calculations from PYTHIA 6.4 (Perugia 2011 Tune) [62,63], PYTHIA 8.1 (Monash 2013 Tune) [52,64], PYTHIA 8.2 (Rope hadronization) [65], EPOS-LHC [66], and HERWIG 7.1 [67], which are shown as different dashed lines. The lower panels show the data to model ratio.

The material budget of the ALICE detector setup is known with an uncertainty of 7% in terms of radiation length, determined on the basis of $\gamma$ conversion measurements [59]. The systematic uncertainty contribution due to material budget is thus estimated by varying the amount of material by ±7% in the Monte Carlo simulation. The systematic uncertainty due to the hadronic interaction cross section in the detector material is estimated by comparing different transport codes: GEANT3 [54], GEANT4 [60], and FLUKA [61]. The effects of material budget and hadronic interactions are evaluated by combining the uncertainties for a pion and a kaon (in case of $K^{*0}$), and for two kaons (in case of $\phi$) according to the kinematics of the decay [28]. These effects are found to be negligible at intermediate and high $p_{\rm T}$ for both $K^{*0}$ and $\phi$.

Raw yield extraction and global tracking efficiency dominate total uncertainties in the lowest and highest $p_{\rm T}$ intervals. The total systematic uncertainties for $K^{*0}$ and $\phi$ amount to 10.9–12.3% (9.1–13.0%) and 6.4–9.2% (5.4–9.5%) in Pb–Pb ($pp$) collisions, respectively. Among the sources of systematic uncertainty, the yield extraction is the only fully uncorrelated source, while track selection, PID, global tracking efficiency, material budget and hadronic interaction are correlated across different centrality classes.

## III. RESULTS

### A. $p_{\rm T}$ spectra in $pp$ collisions

Figure 3 shows the invariant yields of $K^{*0}$ and $\phi$ mesons as a function of $p_{\rm T}$ for inelastic $pp$ collisions at $\sqrt{s}$ = 5.02 TeV. These first measurements at $\sqrt{s}$ = 5.02 TeV extend to

TABLE I. Lévy-Tsallis fit parameters for $K^{*0}$ and $\phi$ meson $p_{\mathrm{T}}$ spectra in $pp$ collisions at $\sqrt{s} = 5.02$ TeV. The errors on the fit parameters result from the total (quadrature sum of statistical and systematic) uncertainties on the data.

| Resonance | $n$ | $C$ (GeV) | $\chi^2$/ndf |
|---|---|---|---|
| $K^{*0}$ | $7.05 \pm 0.14$ | $0.267 \pm 0.006$ | 0.23 |
| $\phi$ | $7.47 \pm 0.16$ | $0.309 \pm 0.006$ | 0.62 |

$p_{\mathrm{T}} = 20$ GeV/$c$ in the rapidity range of $|y| < 0.5$. The shape of both spectra is well described by a Lévy-Tsallis function [68] whose form is given by

$$\frac{d^2N}{dp_{\mathrm{T}}dy} = p_{\mathrm{T}}\frac{dN}{dy}\frac{(n-1)(n-2)}{nC[nC+m(n-2)]}\left[1+\frac{m_{\mathrm{T}}-m}{nC}\right]^{-n}, \quad (5)$$

where $dN/dy$, $n$, and $C$ are the parameters of the function that are determined from the fit to the measured spectra, $m$ is the mass of the hadron, and $m_{\mathrm{T}}$ is the transverse mass defined as $\sqrt{p_{\mathrm{T}}^2 + m^2}$. The Lévy-Tsallis function provides a fair description of the shape of the transverse momentum spectrum over a wide $p_{\mathrm{T}}$ range, thanks to its two parameters: the exponent $n$ and the inverse slope $C$. The parameters obtained from the fit to $K^{*0}$ and $\phi$ spectra in $pp$ collisions at $\sqrt{s} = 5.02$ TeV are given in Table I. They are similar to the parameters obtained in $pp$ collisions at $\sqrt{s} = 7$ and 8 TeV [57]. The $\chi^2$/ndf values are less than unity because the bin-to-bin systematic uncertainties taken in the fit could be correlated. The data are compared to the corresponding results from the QCD inspired Monte Carlo event generators like PYTHIA6 [62], PYTHIA8 [64], HERWIG [67], and EPOS-LHC [66]. In PYTHIA model hadronization of light and heavy quarks is simulated using the Lund string fragmentation model [69]. Various PYTHIA tunes have been developed on the basis of extensive comparisons of Monte Carlo distributions with the minimum bias data from different experiments. Perugia tunes of PYTHIA6 include the revised set of parameters of fragmentation and flavor which improves the overall description of the Tevatron data as well as the reliability of the extrapolations to the LHC measurements [63]. Perugia 2011 takes into account the minimum bias and underlying event data from the LHC at $\sqrt{s} = 0.9$ and 7 TeV. The Monash 2013 Tune of PYTHIA8 uses the updated set of hadronization parameters compared to the previous tunes [52]. It gives an overall good description of kaon data but significantly underestimates the baryon yields at the LHC. The Rope Hadronization model within the framework of PYTHIA8 assumes that instead of independent string fragmentation, the strings overlap to form ropes in the high multiplicity environment [65]. In the Rope Hadronization model, the larger and denser collision systems form color ropes that hadronize with larger string tension leading to enhanced production of strange hadrons with increasing charged particle multiplicity. The HERWIG model includes processes such as coherent parton showers for initial and final state QCD radiation, an eikonal multiple parton-parton interaction model for the underlying event and a cluster hadronization model for the formation of hadrons from the quarks and gluons produced in the parton shower [67]. EPOS-LHC, which is built on the

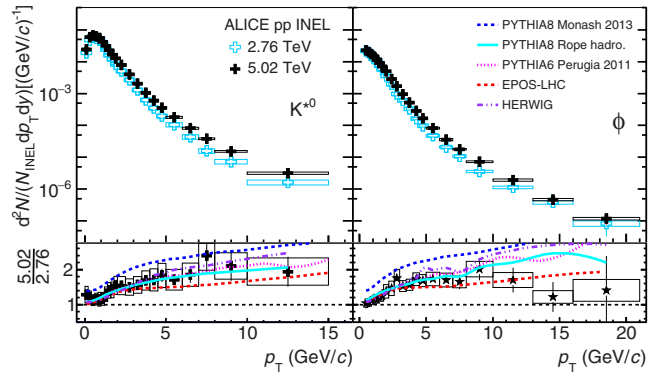


FIG. 4. Comparison of transverse momentum spectra of $K^{*0}$ (left panel) and $\phi$ (right panel) for inelastic $pp$ collisions at $\sqrt{s} = 5.02$ TeV (solid markers) and 2.76 TeV (open markers) [21]. The lower panels show the ratio of the $p_{\mathrm{T}}$ spectra at $\sqrt{s} = 5.02$ TeV to those from $\sqrt{s} = 2.76$ TeV. The statistical uncertainties on the data are shown by bars and the systematic uncertainties by boxes. The ratios are compared with model calculations from the PYTHIA 6.4 (Perugia 2011 Tune) [62,63], PYTHIA 8.1 (Monash 2013 Tune) [52,64], PYTHIA 8.2 (Rope hadronization) [65], EPOS-LHC [66], and HERWIG 7.1 [67], which are shown as different dashed lines.

Parton-Based Gribov Regge Theory, implements a different type of radial flow for $pp$ collisions, where a very dense system is created in a small volume. The model, utilizing the color exchange mechanism of string excitation, is tuned to LHC data [66]. In this model, the part of the collision system that has high string or parton densities becomes a "core" region that may evolve as a quark–gluon plasma; this is surrounded by a more dilute "corona" for which fragmentation occurs as in the vacuum. The strangeness production is higher in the core region that results in strangeness enhancement with increasing multiplicity.

For $K^{*0}$, all the tunes of PYTHIA model overestimate the data for $p_{\mathrm{T}} < 0.5$ GeV/$c$, underestimate the data in the intermediate $p_{\mathrm{T}}$ region and give a better description for $p_{\mathrm{T}} > 10$ GeV/$c$. For $\phi$, all the tunes of PYTHIA model give a better description of the data for $p_{\mathrm{T}} > 10$ GeV/$c$ and underestimate the data for lower $p_{\mathrm{T}}$ region. The deviations in limited $p_{\mathrm{T}}$ ranges observed between data and PYTHIA for both $K^{*0}$ and $\phi$ are similar to those reported for $\sqrt{s} = 2.76$ [21] and 7 TeV [49]. The EPOS-LHC model results are in agreement with the data for $p_{\mathrm{T}} < 5$ GeV/$c$ (3.5 GeV/$c$) and overestimate the data at higher $p_{\mathrm{T}}$ for $K^{*0}$ ($\phi$). HERWIG does not describe the data for both $K^{*0}$ and $\phi$ over the measured $p_{\mathrm{T}}$ region.

Figure 4 shows the comparison of $p_{\mathrm{T}}$ spectra of $K^{*0}$ and $\phi$ mesons between $\sqrt{s} = 5.02$ and 2.76 TeV. The yields of both $K^{*0}$ and $\phi$ mesons are higher at $\sqrt{s} = 5.02$ TeV compared to $\sqrt{s} = 2.76$ TeV. The ratio of the $p_{\mathrm{T}}$ spectra at $\sqrt{s} = 5.02$ to 2.76 TeV as a function of $p_{\mathrm{T}}$ shows that the differential yield ratio increases with $p_{\mathrm{T}}$ for both $K^{*0}$ and $\phi$ mesons and show a hint of saturation at higher $p_{\mathrm{T}}$. These results further help in understanding the nuclear modification factor (derived using $pp$ reference spectra) for Pb–Pb collisions that will be discussed in Sec III E. The ratios are compared to the corresponding calculations from the PYTHIA6 (Perugia 2011

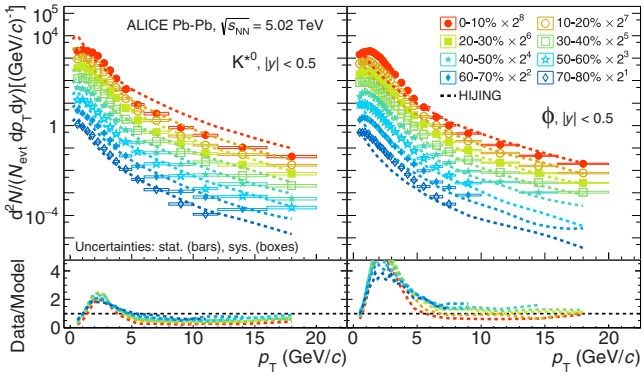


FIG. 5. Transverse momentum spectra of $K^{*0}$ (left panel) and $\phi$ (right panel) at midrapidity in various centrality classes in Pb–Pb collisions at $\sqrt{s_{NN}} = 5.02$ TeV. The statistical uncertainties on the data are shown by bars and the systematic uncertainties by boxes. The results are compared with model calculations from HIJING 1.36 [53], which are shown as dashed lines. The lower panel shows the data to model ratios.

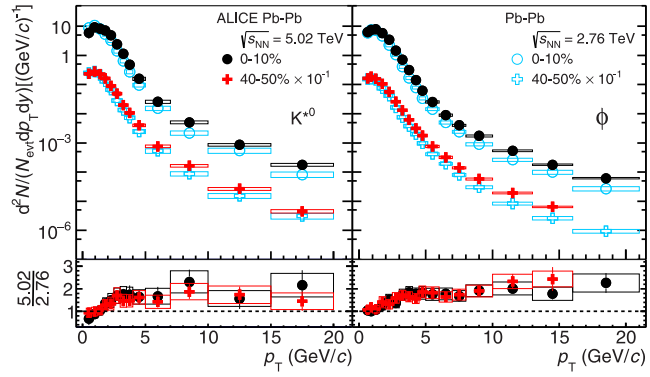


FIG. 6. Comparison of transverse momentum spectra of $K^{*0}$ (left panel) and $\phi$ (right panel) in central (0–10%) and mid-central (40–50%) centrality classes in Pb–Pb collisions at $\sqrt{s_{NN}} = 5.02$ (solid marker) and 2.76 (open marker) TeV [18,21]. The lower panels show the ratio of the $p_T$ spectra at $\sqrt{s_{NN}} = 5.02$ TeV to those from $\sqrt{s_{NN}} = 2.76$ TeV. The statistical uncertainties on the data are shown by bars and the systematic uncertainties by boxes.

Tune), PYTHIA8 (Monash 2013 Tune), PYTHIA8 (Rope hadronization), EPOS-LHC, and HERWIG models. For the $K^{*0}$ meson, all the models except PYTHIA8-Monash 2013 Tune are in good agreement with the measurements within uncertainties for the whole $p_T$ range. For the $\phi$ meson, all the models except PYTHIA8-Monash 2013 Tune are in good agreement with the measurements within uncertainties for $p_T < 8$ GeV/$c$. The ratio of the $p_T$ spectra for $K^{*0}$ and $\phi$ from the Monash 2013 Tune of PYTHIA8 are higher than the measurements for all $p_T$. All the models presented here fail quantitatively and/or qualitatively to describe the $K^{*0}$ and $\phi$ data over the entire measured $p_T$ range. It has proven challenging for event generators to accurately model the $p_T$ distributions of such resonances [21,49,57,58]. Thus, the data and model comparisons may provide valuable inputs to tune the MC event generators so that one get a unified physics description of present results.

### B. $p_T$ spectra in Pb–Pb collisions

Figure 5 shows the $p_T$ distributions for $K^{*0}$ and $\phi$ mesons in Pb–Pb collisions at $\sqrt{s_{NN}} = 5.02$ TeV. The measurements are carried out at midrapidity ($|y| < 0.5$) for eight different centrality classes. For the most central collisions (0–10%), the measurements extend up to $p_T = 20$ GeV/$c$ for both $K^{*0}$ and $\phi$ mesons. The HIJING model was used to calculate the reconstruction efficiency of $K^{*0}$ and $\phi$ mesons in Pb–Pb collisions, hence the data are compared to the corresponding results from the HIJING model [53]. For $K^{*0}$ meson, HIJING does not describe the data for all centrality classes over the whole measured $p_T$ region. For $\phi$ meson, the model gives a good agreement with the data in mid-central collisions for $p_T > 7$ GeV/$c$, however does not describe the data for most of the centrality classes. The $p_T$ spectra are further characterized by the integrated yields ($dN/dy$) and the average transverse momentum ($\langle p_T \rangle$) which are discussed in the next subsection. Figure 6 shows the comparison of the $p_T$ spectra for $K^{*0}$ and $\phi$ mesons in Pb–Pb collisions for the 0–10% and 40–50% centrality classes at $\sqrt{s_{NN}} = 5.02$ and 2.76 TeV. The ratios of the $p_T$ spectra increase with $p_T$ and then tend to saturate at high $p_T$ for both mesons in central as well as in peripheral collisions, as also observed in $pp$ collisions (Fig. 4). These results are useful in understanding the energy dependence of the nuclear modification factor which is discussed in Sec III E. For $p_T > 5.0$ GeV/$c$, the $p_T$ differential yields at 5.02 TeV are ≈1.8 times higher than those measured at 2.76 TeV.

A blast-wave model, which does not include rescattering effects, is used to investigate the $p_T$ dependence of resonance yield suppression. Previously, in Pb–Pb collisions at $\sqrt{s_{NN}} = 2.76$ TeV [18], the $K^{*0}$ and $\phi$ $p_T$ spectra were compared to the expected distributions based on the blast-wave model [40] using parameters obtained from the combined fit to $\pi^{\pm}$, $K^{\pm}$, and $p(\bar{p})$ spectra. A suppression of the $K^{*0}$ yield with respect to the blast-wave distribution was observed for $p_T < 3$ GeV/$c$ in central collisions. This suppression is attributed to rescattering of resonance decay products in the hadronic phase that reduces the measurable yield of $K^{*0}$ mesons [22]. The lack of similar suppression for the $\phi$ meson is interpreted as being due to the absence of rescattering, as it mostly decays outside the fireball because of its longer lifetime. We have carried out a similar exercise for Pb–Pb collisions at $\sqrt{s_{NN}} = 5.02$ TeV. The Boltzmann-Gibbs blast-wave function is a three parameter simplified hydrodynamic model, which assumes that the emitted particles are locally thermalized in a uniform-density source at a kinetic freezeout temperature $T_{\rm kin}$ and move with a common collective transverse radial flow velocity field. It is given by [40]

$$\frac{1}{p_T}\frac{dN}{dp_T} \propto \int_0^R r\, dr\, m_T\, I_0\left(\frac{p_T \sinh\rho}{T_{\rm kin}}\right) K_1\left(\frac{m_T \cosh\rho}{T_{\rm kin}}\right), \tag{6}$$

where $I_0$ and $K_1$ are the modified Bessel functions, $R$ is the fireball radius, and $r$ is the radial distance in the transverse

TABLE II. Blast-wave parameters from fit to charged pion, kaon, and proton spectra in Pb–Pb collisions at $\sqrt{s_{NN}} = 5.02$ TeV.

| Centrality | $T_{\rm kin}$ (GeV) | $\langle\beta_{\rm T}\rangle$ | $n$ |
|---|---|---|---|
| 0–10% | $0.091 \pm 0.003$ | $0.662 \pm 0.003$ | $0.735 \pm 0.013$ |
| 70–80% | $0.147 \pm 0.006$ | $0.435 \pm 0.011$ | $1.678 \pm 0.088$ |

plane. The velocity profile $\rho$ is defined as

$$\rho = \tanh^{-1}\beta_{\rm T}({\rm r}) = \tanh^{-1}\left[\left(\frac{r}{R}\right)^{n}\beta_{\rm s}\right], \tag{7}$$

where $\beta_{\rm T}({\rm r})$ is the transverse expansion velocity and $\beta_{\rm s}$ is the transverse expansion velocity at the surface. The free parameters in the fits are $T_{\rm kin}$, $\beta_{\rm s}$, and the velocity profile exponent $n$. For the current study, the above parameters, listed in Table II, are fixed to the values from fits to the charged pion, kaon, and (anti)proton $p_{\rm T}$ distributions in Pb–Pb collisions at $\sqrt{s_{NN}} =$ 5.02 TeV [27].

Figure 7 shows the expected $K^{*0}$ and $\phi$ $p_{\rm T}$ distributions from the blast-wave model (as solid lines), the measured resonance $p_{\rm T}$ distributions, and the ratios of the measurement to the blast-wave model for central (0–10%) and peripheral (70–80%) collisions. The expected distributions are normalized so that their integrals are equal to the measured yield of charged kaons in Pb–Pb collisions at $\sqrt{s_{NN}} = 5.02$ TeV [27] multiplied by the $K^{*0}/K$ and $\phi/K$ ratios from $pp$ collisions at $\sqrt{s} =$ 5.02 TeV. A similar procedure of normalization was used in Pb–Pb collisions at $\sqrt{s_{NN}} = 2.76$ TeV [18]. The ratio for the $\phi$ meson $p_{\rm T}$ distribution is close to unity and no significant differences are observed in central or peripheral collisions for $p_{\rm T} < 2$ GeV/$c$. However, the data/blast-wave ratio for the $K^{*0}$ is lower than unity with a deviation of 40–60% for $p_{\rm T} < 3$ GeV/$c$ in central collisions. In peripheral collisions, the data/blast-wave ratio for the $K^{*0}$ shows a significantly smaller deviation from unity for $p_{\rm T} < 2$ GeV/$c$ relative to central collisions. Both $K^{*0}$ and $\phi$ show a similar deviation

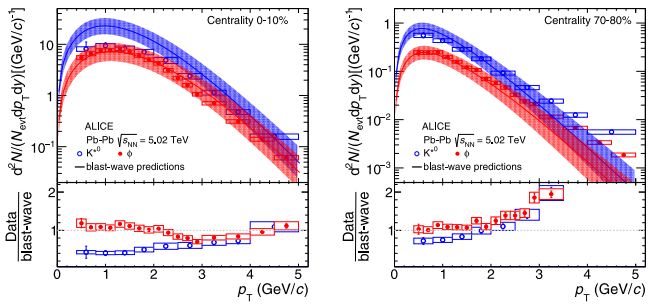


FIG. 7. Transverse-momentum distributions of $K^{*0}$ and $\phi$ resonances in Pb–Pb collisions at $\sqrt{s_{NN}} = 5.02$ TeV along with expected distributions for central (left) and peripheral (right) collisions. The shapes of the expected distributions are given by Boltzmann-Gibbs blast-wave functions [40] using parameters obtained from fits to pion, kaon, and (anti)proton $p_{\rm T}$ distributions [27] (see text for details). The shaded bands indicate the uncertainties in the fit parameters of the model distributions. The lower panels show the ratios of the measured distribution to the values from the model.

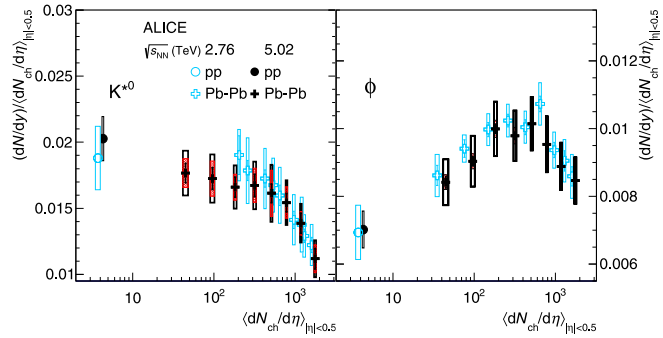


FIG. 8. Transverse momentum integrated yield ($dN/dy$) of $K^{*0}$ and $\phi$ as a function of the averaged charged particle density ($\langle dN_{\rm ch}/d\eta\rangle_{|\eta|<0.5}$) in $pp$ and Pb–Pb collisions at $\sqrt{s_{NN}} = 5.02$ TeV and compared with result from Pb–Pb collisions at $\sqrt{s_{NN}} = 2.76$ TeV [18,21]. The statistical uncertainties on the data are shown by bars and the systematic uncertainties by boxes. The shaded box shows the uncorrelated systematic uncertainties.

for $p_{\rm T} > 3$ GeV/$c$ (>2.5 GeV/$c$) in central (peripheral) collisions. The blast-wave model is expected to describe the measured $p_{\rm T}$ distributions over the entire $p_{\rm T}$ range if these are driven purely by the collective radial expansion of the system. The model describes the data over a wider $p_{\rm T}$ interval for central Pb–Pb collisions than for peripheral collisions as observed for $\pi$, $K$, $p$ in Pb–Pb collisions at $\sqrt{s_{NN}} = 5.02$ TeV [27]. For Pb–Pb collisions, the average transverse velocity $\langle\beta_{\rm T}\rangle$ is observed to increase with centrality while $T_{\rm kin}$ decreases [27]. For central Pb–Pb collisions, the shape of the $p_{\rm T}$ distributions of $K^{*0}$ and $\phi$ mesons for $p_{\rm T} < 2$ GeV/$c$ are consistent with the blast-wave parameterization within uncertainties. The suppression of yields of $K^{*0}$ with respect to the blast-wave model expectation in central collisions, relative to peripheral collisions and $\phi$ mesons, is consistent with the dominance of rescattering effects in the medium formed in Pb–Pb collisions at $\sqrt{s_{NN}} = 5.02$ TeV.

### C. $dN/dy$ and $\langle p_{\rm T}\rangle$

Figure 8 shows the $p_{\rm T}$-integrated yield $dN/dy$ of $K^{*0}$ and $\phi$ mesons scaled by the average charged particle multiplicity measured at midrapidity ($\langle dN_{\rm ch}/d\eta\rangle_{|\eta|<0.5}$) as a function of $\langle dN_{\rm ch}/d\eta\rangle_{|\eta|<0.5}$ for Pb–Pb and $pp$ collisions at $\sqrt{s_{NN}} =$ 5.02 TeV. The $p_{\rm T}$-integrated yields ($dN/dy$) have been obtained by integrating the spectra over $p_{\rm T}$ using the measured data and a blast-wave function (Lévy-Tsallis function) in the unmeasured regions for Pb–Pb ($pp$) collisions. The fraction of the yields from the extrapolation to the total for $K^{*0}$ ($\phi$) mesons is 0.09 (0.08) in the 0–10% centrality class, and is 0.16 (0.12) in the 70–80% centrality class. This fraction is 0.17 for $\phi$ in $pp$, whereas no extrapolation is needed for $K^{*0}$. For comparison, the corresponding results from $\sqrt{s_{NN}} = 2.76$ TeV are also shown in Fig. 8. The dependence of the normalized $dN/dy$ on $\langle dN_{\rm ch}/d\eta\rangle$ is found to be the same regardless of the beam energy.

The average transverse momentum $\langle p_{\rm T}\rangle$ values for the $K^{*0}$ and $\phi$ resonances are obtained by using the data in the measured region and a blast-wave function (Lévy-Tsallis function)

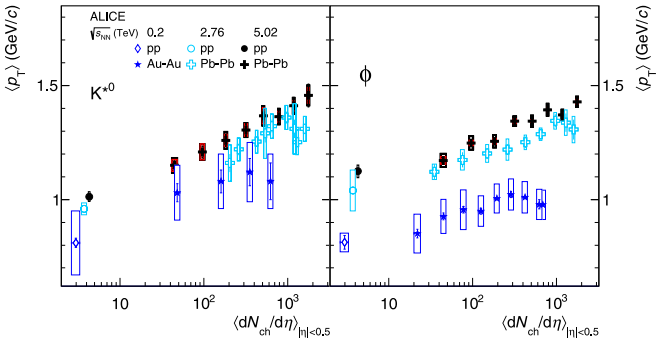


FIG. 9. Mean transverse momentum of $K^{*0}$ and $\phi$ as a function of the averaged charged particle density ($\langle dN_{\rm ch}/d\eta\rangle_{|\eta|<0.5}$) in Pb–Pb and $pp$ collisions at $\sqrt{s_{NN}} = 5.02$ TeV. Also shown for comparison are the corresponding values from Pb–Pb and $pp$ collisions at $\sqrt{s_{NN}} =$ 2.76 TeV [18,21], and Au–Au and $pp$ collisions at $\sqrt{s_{NN}} = 200$ GeV [9,10,12,13]. The statistical uncertainties on the data are shown by bars and the systematic uncertainties by boxes. The shaded box shows the uncorrelated systematic uncertainties.

in the unmeasured regions for Pb–Pb ($pp$) collisions. Figure 9 shows $\langle p_{\rm T}\rangle$ values obtained at midrapidity ($|y| < 0.5$) as a function of $\langle dN_{\rm ch}/d\eta\rangle_{|\eta|<0.5}$ for Pb–Pb and $pp$ collisions at $\sqrt{s_{NN}} = 5.02$ TeV. The $\langle p_{\rm T}\rangle$ values increase with charged particle multiplicity. The $\langle p_{\rm T}\rangle$ of $K^{*0}$ and $\phi$ mesons, which have similar masses, are similar for events with the same $\langle dN_{\rm ch}/d\eta\rangle_{|\eta|<0.5}$ in Pb–Pb collisions. Both of these features are consistent with the picture of a growing contribution of radial flow with increasing $\langle dN_{\rm ch}/d\eta\rangle_{|\eta|<0.5}$ for the system formed in Pb–Pb collisions at $\sqrt{s_{NN}} = 5.02$ TeV [27]. These results are also compared to the corresponding results from Pb–Pb collisions at $\sqrt{s_{NN}} = 2.76$ TeV [18,21], and to Au–Au and $pp$ collisions at $\sqrt{s_{NN}} = 200$ GeV [9,10,12,13]. The $\langle p_{\rm T}\rangle$ values are larger for higher energy collisions at similar values of $\langle dN_{\rm ch}/d\eta\rangle_{|\eta|<0.5}$, although the uncertainties are also larger at lower collision energies for $K^{*0}$. The qualitative features of the dependence of $K^{*0}$ and $\phi$ meson $\langle p_{\rm T}\rangle$ on $\langle dN_{\rm ch}/d\eta\rangle_{|\eta|<0.5}$ are similar at RHIC and LHC energies. The values of $dN/dy$ and $\langle p_{\rm T}\rangle$ of $K^{*0}$ and $\phi$ measured in Pb–Pb and $pp$ collisions at $\sqrt{s_{NN}} = 5.02$ TeV are given in Table III.

Figure 10 compares the $\langle p_{\rm T}\rangle$ of $K^{*0}$ and $\phi$ as a function of $\langle dN_{\rm ch}/d\eta\rangle_{|\eta|<0.5}$ with the respective values for $\pi^{\pm}$, $K^{\pm}$, and $p(\bar{p})$ [27] for Pb–Pb collisions at $\sqrt{s_{NN}} = 5.02$ TeV. All the hadrons exhibit an increase in $\langle p_{\rm T}\rangle$ from peripheral to central Pb–Pb collisions: the largest increase is observed for protons, followed by the $K^{*0}$ and $\phi$ mesons, and then by K and $\pi$. The rise in the $\langle p_{\rm T}\rangle$ values is steeper for hadrons with higher mass, as expected in presence of a radial flow effect. For $\langle dN_{\rm ch}/d\eta\rangle_{|\eta|<0.5} > 300$, the $\langle p_{\rm T}\rangle$ values of $K^{*0}$, $p$, and $\phi$ hadrons follow a similar trend and have quantitatively similar values within uncertainties at a given $\langle dN_{\rm ch}/d\eta\rangle_{|\eta|<0.5}$ value. The masses of these hadrons are similar, $K^{*0} \approx 896$ MeV/$c^2$, $p \approx 938$ MeV/$c^2$, and $\phi \approx 1019$ MeV/$c^2$. The hadron mass

TABLE III. The values of $dN/dy$ and $\langle p_{\rm T}\rangle$ measured in Pb–Pb and pp collisions at $\sqrt{s_{NN}} = 5.02$ TeV. Pb–Pb results are shown for the different centrality classes. In each entry the first uncertainty is statistical and the second one is systematic.

| | $K^{*0}$ | |
|---|---|---|
| Centrality class | $dN/dy$ | $\langle p_{\rm T}\rangle$ |
| 0–10% | 19.726 ± 1.357 ± 2.475 | 1.457 ± 0.053 ± 0.044 |
| 10–20% | 16.363 ± 0.895 ± 1.725 | 1.411 ± 0.039 ± 0.035 |
| 20–30% | 12.129 ± 0.547 ± 1.331 | 1.364 ± 0.031 ± 0.034 |
| 30–40% | 8.260 ± 0.361 ± 1.111 | 1.368 ± 0.030 ± 0.043 |
| 40–50% | 5.321 ± 0.268 ± 0.574 | 1.305 ± 0.034 ± 0.032 |
| 50–60% | 3.039 ± 0.140 ± 0.300 | 1.259 ± 0.030 ± 0.037 |
| 60–70% | 1.661 ± 0.079 ± 0.176 | 1.209 ± 0.028 ± 0.035 |
| 70–80% | 0.793 ± 0.033 ± 0.076 | 1.150 ± 0.024 ± 0.033 |
| | $\phi$ | |
| Centrality class | $dN/dy$ | $\langle p_{\rm T}\rangle$ |
| 0–10% | 14.937 ± 0.154 ± 1.210 | 1.429 ± 0.008 ± 0.023 |
| 10–20% | 10.483 ± 0.113 ± 0.828 | 1.371 ± 0.008 ± 0.024 |
| 20–30% | 7.497 ± 0.083 ± 0.647 | 1.393 ± 0.009 ± 0.027 |
| 30–40% | 5.192 ± 0.056 ± 0.404 | 1.344 ± 0.008 ± 0.024 |
| 40–50% | 3.113 ± 0.038 ± 0.237 | 1.343 ± 0.009 ± 0.021 |
| 50–60% | 1.829 ± 0.024 ± 0.148 | 1.256 ± 0.010 ± 0.027 |
| 60–70% | 0.870 ± 0.013 ± 0.072 | 1.248 ± 0.011 ± 0.029 |
| 70–80% | 0.378 ± 0.008 ± 0.031 | 1.171 ± 0.014 ± 0.029 |
| | $pp$ collisions | |
| Particle specie | $dN/dy$ | $\langle p_{\rm T}\rangle$ |
| $K^{*0}$ | 0.0872 ± 0.0006 ± 0.0072 | 1.0131 ± 0.0038 ± 0.0216 |
| $\phi$ | 0.0302 ± 0.0002 ± 0.0024 | 1.1239 ± 0.0047 ± 0.0282 |

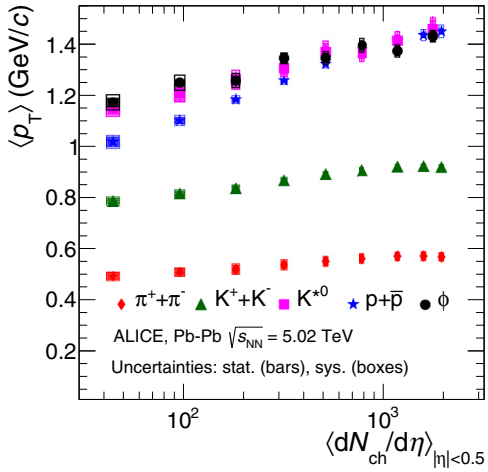


FIG. 10. Mean transverse momentum of $K^{*0}$ and $\phi$ as a function of the averaged charged particle density ($\langle dN_{ch}/d\eta \rangle_{|\eta|<0.5}$) in Pb–Pb collisions at $\sqrt{s_{NN}} = 5.02$ TeV compared with the corresponding values for other identified particles such as $\pi^{\pm}$, $K^{\pm}$, and $p(\bar{p})$ [27]. The statistical uncertainties on the data are shown by bars and the systematic uncertainties by boxes. The shaded boxes show the uncorrelated systematic uncertainties.

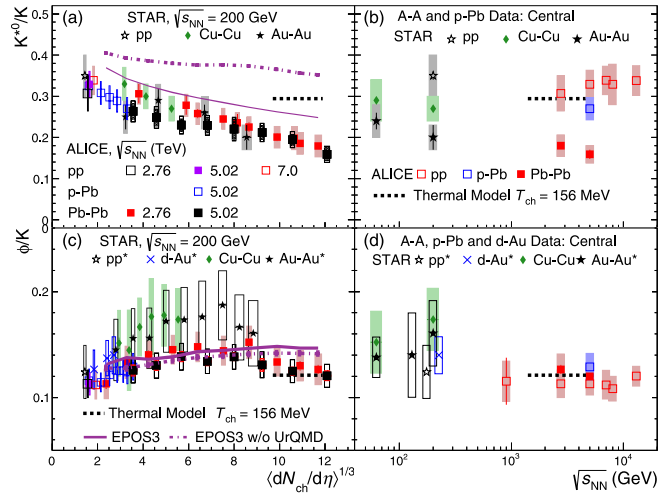


FIG. 11. Particle ratios $K^{*0}/K$ [panels (a) and (b)] and $\phi/K$ [panels (c) and (d)] in $pp$, d–Au, $p$-Pb, Cu–Cu, Au–Au, and Pb–Pb collisions [9,10,12–14,18,21,49–51,70]. In panels (a) and (c) these ratios are presented as a function of $\langle dN_{ch}/d\eta \rangle^{1/3}$. These ratios are measured as $K^{*0}/K^-$ and $\phi/K^-$ in Pb–Pb collisions at $\sqrt{s_{NN}} =$ 2.76 TeV and in STAR experiment. The values of $\langle dN_{ch}/d\eta \rangle_{|\eta|<0.5}$ were measured at midrapidity. In panels (b) and (d), these ratios are presented for $pp$, central d–Au, $p$-Pb, and heavy-ion collisions as a function of $\sqrt{s_{NN}}$. The values given by a grand-canonical thermal model with a chemical freezeout temperature of 156 MeV are also shown [39]. For quantities marked "*", boxes represent the total uncertainty (separate uncertainties are not reported). Otherwise, bars represent the statistical uncertainties and boxes represent the systematic uncertainties (including centrality-uncorrelated and centrality-correlated components). EPOS3 model predictions [20] of $K^{*0}/K$ and $\phi/K$ ratios in Pb–Pb collisions are also shown as violet lines.

dependence of $\langle p_T \rangle$ is consistent with the expectation from a hydrodynamic evolution of the system formed in Pb–Pb collisions at $\sqrt{s_{NN}} = 5.02$ TeV for $\langle dN_{ch}/d\eta \rangle_{|\eta|<0.5} > 300$. In peripheral collisions ($\langle dN_{ch}/d\eta \rangle_{|\eta|<0.5} < 300$), $\langle p_T \rangle$ of proton is lower than those of $K^{*0}$ and $\phi$, indicating the breaking of mass ordering while going toward peripheral Pb–Pb collisions.

### D. Particle ratios

Figure 11 shows the $K^{*0}/K$ ratio in panels (a) and (b) for different collision systems at RHIC [9,10,12–14,49] and at the LHC [18,21,50,51,70] as a function of $\langle dN_{ch}/d\eta \rangle^{1/3}$ and $\sqrt{s_{NN}}$, respectively. The $K^{*0}/K$ ratio in heavy-ion collisions is smaller than those in $pp$ collisions, with the results from $p$-Pb lying in between. The $K^{*0}/K$ ratio decreases when the system size increases, as reflected by the values of $\langle dN_{ch}/d\eta \rangle^{1/3}$ (a proxy for system size [42]). To quantify the suppression of $K^{*0}/K$ ratio in central Pb–Pb collisions with respect to $pp$ collisions, we calculate the double ratio $(K^{*0}/K)_{PbPb}/(K^{*0}/K)_{pp}$. The $K^{*0}/K$ double ratio in Pb–Pb collisions at 5.02 TeV (2.76 TeV) is $0.483 \pm 0.082$ ($0.585 \pm 0.122$), which deviates from unity by 6.2 (3.4) times its standard deviation. The same ratio in Au–Au collisions at $\sqrt{s_{NN}} = 200$ GeV gives $0.571 \pm 0.147$, which deviates from unity by 2.9 times its standard deviation. Figure 11(b) shows $K^{*0}/K$ ratio as a function of $\sqrt{s_{NN}}$ for $pp$ collisions, as well as for central $p$-Pb, Cu–Cu, Au–Au, and Pb–Pb collisions. The $K^{*0}/K$ ratio is higher in $pp$ collisions than in central Au–Au and Pb–Pb collisions at various center of mass energies. The value of the $K^{*0}/K$ ratio is larger in central Cu–Cu than in central Au–Au collisions, as expected because of the smaller Cu–Cu system size.

Figures 11(c) and 11(d) show the $\phi/K$ ratio for different collision systems at RHIC [9,10,12–14,49] and LHC [18,21,50,51,70] as a function of $\langle dN_{ch}/d\eta \rangle^{1/3}$ and $\sqrt{s_{NN}}$, respectively. In contrast to the $K^{*0}/K$ ratio, the $\phi/K$ ratio is approximately constant as a function of $\langle dN_{ch}/d\eta \rangle^{1/3}$. The values of the $\phi/K$ ratio in Au–Au and Cu–Cu collisions are slightly larger than the corresponding results from Pb–Pb collisions, but agree within uncertainties. The $\phi/K$ ratio is found to be independent of collision energy and system from RHIC to LHC energies.

Figures 11(a) and 11(c) also show the $K^{*0}/K$ and $\phi/K$ ratios from EPOS3 model calculations with and without a hadronic cascade phase modeled by UrQMD [20], and thermal model calculations with chemical freezeout temperature $T_{ch} = 156$ MeV [39]. The thermal or statistical hadronization model assumes that the system formed in heavy-ion collisions reaches thermal equilibrium through multiple interactions and undergoes a rapid expansion followed by the chemical freezeout. The freezeout surface is characterized by three parameters: the chemical freezeout temperature $T_{ch}$, the chemical potential $\mu$ and the fireball volume V. The value of the $K^{*0}/K$ ratio in central Pb–Pb collisions is smaller than the thermal model expectation, however $\phi/K$ ratio is in fair agreement with the model calculations. The EPOS3 event generator is based on 3 + 1D viscous hydrodynamical evolution where the initial stage is treated via multiple scattering approach based on Pomerons and strings and the reaction

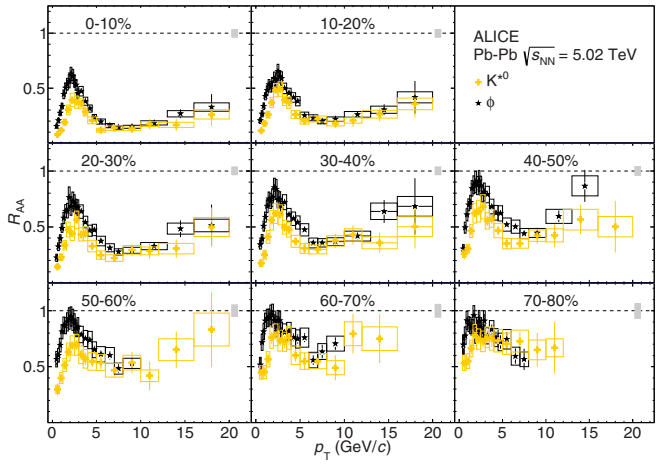


FIG. 12. The nuclear modification factor, $R_{AA}$, as a function of $p_T$ for $K^{*0}$ and $\phi$ mesons at midrapidity ($|y| < 0.5$) for different centrality classes in Pb–Pb collisions at $\sqrt{s_{NN}} = 5.02$ TeV. The statistical and systematic uncertainties are shown as bars and boxes, respectively. The boxes around unity indicate the uncertainty on the normalization of $R_{AA}$.

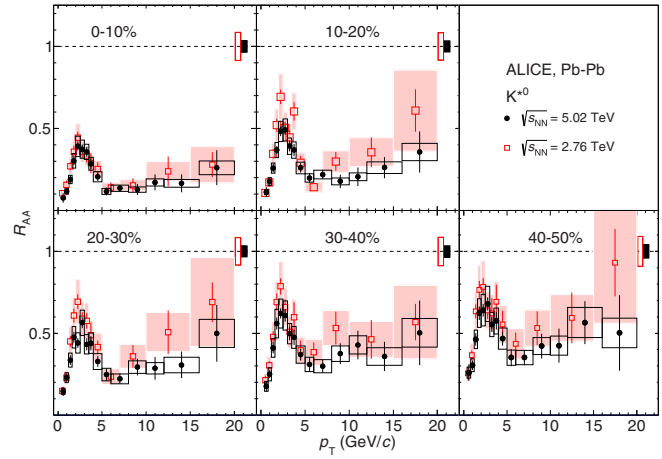


FIG. 13. The nuclear modification factor, $R_{AA}$, as a function of $p_T$ for $K^{*0}$ for different centrality classes in Pb–Pb collisions at $\sqrt{s_{NN}} = 5.02$ TeV compared with the results from Pb–Pb collisions at $\sqrt{s_{NN}} = 2.76$ TeV [21]. The statistical and systematic uncertainties are shown as bars and boxes, respectively. The boxes around unity indicate the respective uncertainty on the normalization of $R_{AA}$.

volume is divided into two parts, "core" and "corona." It is the core part that provides the initial condition for QGP evolution, described by viscous hydrodynamics. The corona part is composed of hadrons from the string decays. In EPOS3 + UrQMD approach [20], the hadrons separately produced from core and corona parts are fed into UrQMD [71,72], which describes the hadronic interactions in a microscopic approach. The chemical and kinetic freezeouts occur during this phase. The model predictions from EPOS3 and EPOS3 + UrQMD are shown for Pb–Pb collisions at $\sqrt{s_{NN}} = 2.76$ TeV. As the ratios are shown as a function of $\langle dN_{\rm ch}/d\eta \rangle$, no significant qualitative differences are expected between the two energies. The observed trends of the $K^{*0}/K$ and $\phi/K$ ratios are reproduced by the EPOS3 generator with UrQMD. However, EPOS3 model without hadronic interactions is unable to reproduce the suppression of $K^{*0}/K$ ratios toward the higher $\langle dN_{\rm ch}/d\eta \rangle^{1/3}$ values or central collisions.

### E. Nuclear modification factor

The nuclear modification factor, $R_{AA}$, of $K^{*0}$ and $\phi$ mesons are studied as a function of centrality and center-of-mass energy. The $R_{AA}$ values of resonances are also compared to those of $\pi$, $K$, and $p$ to investigate the hadron species dependence of $R_{AA}$.

#### *1. Centrality dependence of the nuclear modification factor*

The centrality dependence of $R_{AA}$ helps in understanding the evolution of parton energy loss in the medium as a function of the system size. Figure 12 shows the $R_{AA}$ for $K^{*0}$ and $\phi$ mesons as a function of $p_T$ for different centrality classes at midrapidity ($|y| < 0.5$) for Pb–Pb collisions at $\sqrt{s_{NN}} = 5.02$ TeV. The $R_{AA}$ values are lower for $K^{*0}$ compared to $\phi$ for $p_T < 5$ GeV/$c$ for most of the collision centralities studied. This can be attributed to the dominance of rescattering effects at lower $p_T$. At higher $p_T$ ($> 6$ GeV/$c$) the $R_{AA}$ values for $K^{*0}$ and $\phi$ mesons are comparable within uncertainties. The $R_{AA}$ values below unity at high $p_T$ support the picture of a suppression of high $p_T$ hadron production due to parton energy loss in the medium formed in heavy-ion collisions. For all the collision centralities studied, the $R_{AA}$ values are below unity and the values increase for $p_T > 6$ GeV/$c$. The average $R_{AA}$ values at high $p_T$ ($> 6$ GeV/$c$) are found to decrease when going from peripheral to central collisions for both $K^{*0}$ and $\phi$ mesons. The dependence of $R_{AA}$ on collision centrality at high $p_T$ provides information on the path length dependence of parton energy loss in the medium formed in high energy heavy-ion collisions [21,31,73–76]. This is reflected as a more pronounced suppression of $R_{AA}$ in the most central collisions, as expected from the longer path length traversed by the hard partons as they lose energy via multiple interactions.

#### *2. Center-of-mass energy dependence of the nuclear modification factor*

Figure 13 (Figure 14) show the $p_T$-differential $R_{AA}$ for the $K^{*0}$ ($\phi$) meson for five different collision centrality classes (0–10%, 10–20%, 20–30%, 30–40%, and 40–50%) in Pb–Pb collisions. The $R_{AA}$ values for $\sqrt{s_{NN}} = 5.02$ TeV are compared to the corresponding values at $\sqrt{s_{NN}} = 2.76$ TeV. No significant differences are observed between 5.02 and 2.76 TeV for both the $K^{*0}$ and $\phi$ resonances. This is supported by Figs. 4 and 6, which show that the ratios of $p_T$ spectra of $K^{*0}$ and $\phi$ at 5.02 TeV to that at 2.76 TeV are similar for both $pp$ and Pb–Pb collisions. The results from Figs. 12–14 indicate that within uncertainties, the nuclear modification factor is independent of the resonance species at high $p_T$ and compatible with measurements at $\sqrt{s_{NN}} = 2.76$ TeV for different centrality classes. However, the $R_{AA}$ measurements of other mesonic and baryonic resonances like $\rho(770)^0$, $\Delta(1232)^{++}$, $\Sigma(1385)$, and

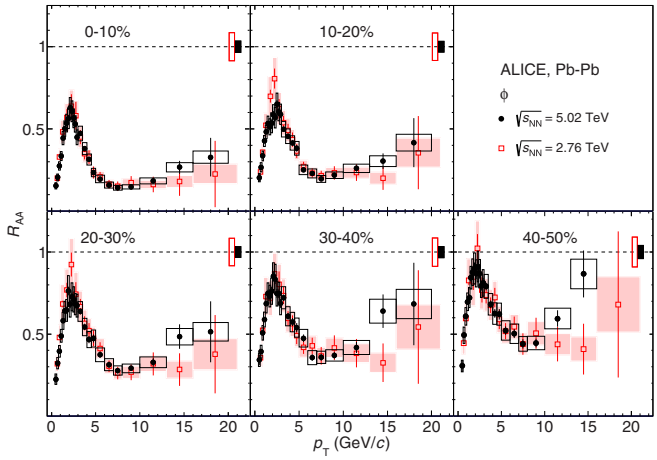


FIG. 14. The nuclear modification factor, $R_{AA}$, as a function of $p_{\mathrm{T}}$ for $\phi$ mesons in different centrality classes in Pb–Pb collisions at $\sqrt{s_{NN}} = 5.02$ TeV compared with the results in Pb–Pb collisions at $\sqrt{s_{NN}} = 2.76$ TeV [21]. The statistical and systematic uncertainties are shown as bars and boxes, respectively. The boxes around unity indicate the uncertainty on the normalization of $R_{AA}$.

$\Lambda(1520)$ which differ in lifetime, mass, quark content, and particle type are required to further support these results.

### *3. Hadron species dependence of the nuclear modification factor*

Figure 15 shows the hadron species dependence of $R_{AA}$ for various collision centrality classes in Pb–Pb collisions at $\sqrt{s_{NN}} = 5.02$ TeV. The hadron species considered here are charged pions, kaons, (anti)protons, $K^{*0}$ and $\phi$ mesons. They vary in mass from about 140 to 1019 MeV, both baryons and mesons are considered, and their valence quark contents are also different. At low $p_{\mathrm{T}}$ (<2 GeV/$c$), the $K^{*0}$ $R_{AA}$ values are the smallest for central collisions; this is attributed to the rescattering effect as discussed earlier in the article. For the $p_{\mathrm{T}}$ range 2–8 GeV/$c$, there appears to be a hadron mass dependence for mesons. It is also observed that $R_{AA}$ of proton is higher than all mesons including $\phi$. This indicate a baryon-meson ordering. So, even in the presence of strong radial flow in this $p_{\mathrm{T}}$ region, there are other effects which can affect $R_{AA}$. For $p_{\mathrm{T}}$ larger than 8 GeV/$c$, all the particle species show similar $R_{AA}$ values within uncertainties for all the collision centralities studied. This suggests that, despite the varying degree of energy loss at different collision centralities, the relative particle composition at high $p_{\mathrm{T}}$ remains the same as in vacuum.

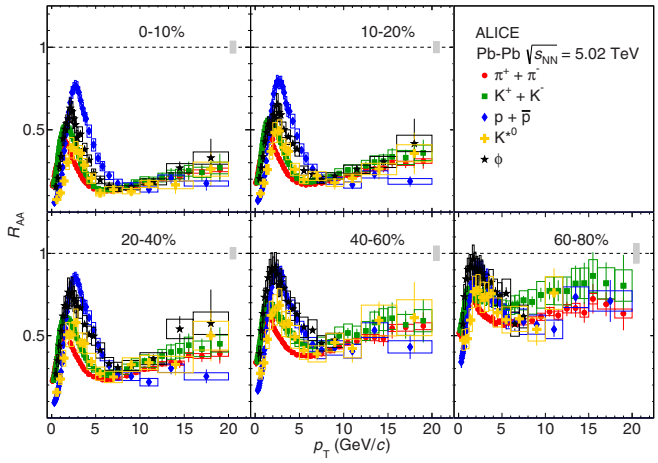


FIG. 15. The nuclear modification factor, $R_{AA}$, as a function of $p_{\mathrm{T}}$ for $K^{*0}$ and $\phi$ mesons in Pb–Pb collisions for different centrality classes at $\sqrt{s_{NN}} = 5.02$ TeV. The results are compared with the $R_{AA}$ values of $\pi$, $K$, and $p$ measured by ALICE [27]. The statistical and systematic uncertainties are shown as bars and boxes, respectively. The boxes around unity indicate the uncertainty on the normalization of $R_{AA}$.

## IV. CONCLUSIONS

The transverse momentum distributions of $K^{*0}$ and $\phi$ mesons have been measured in inelastic $pp$ and Pb–Pb collisions at $\sqrt{s_{NN}} = 5.02$ TeV using the ALICE detector. The measurements are carried out at midrapidity ($|y| < 0.5$) up to $p_{\mathrm{T}} = 20$ GeV/$c$ and for Pb–Pb collisions in various collision centrality classes.

The $p_{\mathrm{T}}$ distributions for $K^{*0}$ and $\phi$ mesons in $pp$ collisions are well described by a Lévy-Tsallis function and are compared to results from the PYTHIA6, PYTHIA8, EPOS-LHC, and HERWIG event generators. None of the models are able to describe the transverse momentum distributions of $K^{*0}$ and $\phi$ in the measured $p_{\mathrm{T}}$ range. The $\langle p_{\mathrm{T}} \rangle$ values are found to increase with $\langle dN_{\mathrm{ch}}/d\eta \rangle_{|\eta|<0.5}$, with the mass of the hadron and with $\sqrt{s_{NN}}$. These measurements are consistent with the observation that radial flow effects are larger for more central collisions and increased high-$p_{\mathrm{T}}$ production at higher collision energies.

The $p_{\mathrm{T}}$-integrated particle ratios as a function of $\sqrt{s_{NN}}$ and $\langle dN_{\mathrm{ch}}/d\eta \rangle^{1/3}$ in Pb–Pb and inelastic $pp$ collisions have been compared. The $K^{*0}/K$ and $\phi/K$ ratios as a function of $\sqrt{s_{NN}}$ and $\langle dN_{\mathrm{ch}}/d\eta \rangle^{1/3}$ taken together indicate the dominance of the rescattering effect in the hadronic phase in Pb–Pb collisions. EPOS3 and thermal models that do not include hadronic interactions are unable to describe the suppression of $K^{*0}/K$ ratio. EPOS3 + UrQMD, where the hadronic phase is described by the UrQMD model, is able to reproduce the decreasing trend of $K^{*0}/K$ ratio as a function of multiplicity in the Pb–Pb collisions. In contrast, the $\phi/K$ ratios in Pb–Pb collisions are quite comparable to those from $pp$ collisions, and agree well with all model calculations. The dissimilarity in the behavior of $K^{*0}/K$ and $\phi/K$ ratios is dominantly attributed to the lifetime of $K^{*0}$, which is a factor of 10 smaller than the lifetime of the $\phi$ meson. Hence, $K^{*0}$ decay daughters are subjected to a greater rescattering in the hadronic medium. The comparison of transverse momentum distributions of $K^{*0}$ and $\phi$ in central Pb–Pb collisions with blast-wave predictions, which does not include rescattering effects, show a suppression of $K^{*0}$ yield for $p_{\mathrm{T}} < 3$ GeV/$c$.

At low $p_{\mathrm{T}}$ ($< 5$ GeV/$c$), the nuclear modification factor values for $K^{*0}$ are lower with respect to those obtained for $\phi$ mesons, chiefly because of rescattering effects. The $R_{AA}$ values at high $p_{\mathrm{T}}$ ($>$ 6–8 GeV/$c$) for $K^{*0}$ and $\phi$ mesons are comparable within uncertainties. The average $R_{AA}$ values

at high $p_T$ are found to decrease when going from peripheral to central collisions. The $R_{AA}$ values at high $p_T$ for $K^{*0}$ and $\phi$ mesons at $\sqrt{s_{NN}} = 5.02$ TeV are comparable to the corresponding measurements at $\sqrt{s_{NN}} = 2.76$ TeV for most of the collision centralities studied. At the same time, the transverse momentum spectra at high $p_T$ in both $pp$ and Pb–Pb collisions are found to be higher by a factor of about 1.8 at $\sqrt{s_{NN}} = 5.02$ TeV compared to $\sqrt{s_{NN}} = 2.76$ TeV. Further, we find that the $R_{AA}$ values at high $p_T$ for the hadrons $\pi$, $K$, $K^{*0}$, $p$, and $\phi$ are similar within uncertainties for all the collision centrality classes studied. This suggests that the energy loss in the medium which leads to the suppression does not modify the particle composition in the light quark sector.

## ACKNOWLEDGMENTS

The ALICE Collaboration thanks all its engineers and technicians for their invaluable contributions to the construction of the experiment and the CERN accelerator teams for the outstanding performance of the LHC complex. The ALICE Collaboration gratefully acknowledges the resources and support provided by all Grid centres and the Worldwide LHC Computing Grid (WLCG) collaboration. The ALICE Collaboration acknowledges the following funding agencies for their support in building and running the ALICE detector: A. I. Alikhanyan National Science Laboratory (Yerevan Physics Institute) Foundation (ANSL), State Committee of Science and World Federation of Scientists (WFS), Armenia; Austrian Academy of Sciences, Austrian Science Fund (FWF): [M 2467-N36] and Nationalstiftung für Forschung, Technologie und Entwicklung, Austria; Ministry of Communications and High Technologies, National Nuclear Research Center, Azerbaijan; Conselho Nacional de Desenvolvimento Científico e Tecnológico (CNPq), Financiadora de Estudos e Projetos (Finep), Fundação de Amparo à Pesquisa do Estado de São Paulo (FAPESP) and Universidade Federal do Rio Grande do Sul (UFRGS), Brazil; Ministry of Education of China (MOEC), Ministry of Science & Technology of China (MSTC) and National Natural Science Foundation of China (NSFC), China; Ministry of Science and Education and Croatian Science Foundation, Croatia; Centro de Aplicaciones Tecnológicas y Desarrollo Nuclear (CEADEN), Cubaenergía, Cuba; Ministry of Education, Youth and Sports of the Czech Republic, Czech Republic; The Danish Council for Independent Research | Natural Sciences, the VILLUM FONDEN and Danish National Research Foundation (DNRF), Denmark; Helsinki Institute of Physics (HIP), Finland; Commissariat à l'Energie Atomique (CEA) and Institut National de Physique Nucléaire et de Physique des Particules (IN2P3) and Centre National de la Recherche Scientifique (CNRS), France; Bundesministerium für Bildung und Forschung (BMBF) and GSI Helmholtzzentrum für Schwerionenforschung GmbH, Germany; General Secretariat for Research and Technology, Ministry of Education, Research and Religions, Greece; National Research, Development and Innovation Office, Hungary; Department of Atomic Energy Government of India (DAE), Department of Science and Technology, Government of India (DST), University Grants Commission, Government of India (UGC) and Council of Scientific and Industrial Research (CSIR), India; Indonesian Institute of Science, Indonesia; Istituto Nazionale di Fisica Nucleare (INFN), Italy; Institute for Innovative Science and Technology, Nagasaki Institute of Applied Science (IIST), Japanese Ministry of Education, Culture, Sports, Science and Technology (MEXT) and Japan Society for the Promotion of Science (JSPS) KAKENHI, Japan; Consejo Nacional de Ciencia (CONACYT) y Tecnología, through Fondo de Cooperación Internacional en Ciencia y Tecnología (FONCICYT) and Dirección General de Asuntos del Personal Academico (DGAPA), Mexico; Nederlandse Organisatie voor Wetenschappelijk Onderzoek (NWO), Netherlands; The Research Council of Norway, Norway; Commission on Science and Technology for Sustainable Development in the South (COMSATS), Pakistan; Pontificia Universidad Católica del Perú, Peru; Ministry of Education and Science, National Science Centre and WUT ID-UB, Poland; Korea Institute of Science and Technology Information and National Research Foundation of Korea (NRF), Republic of Korea; Ministry of Education and Scientific Research, Institute of Atomic Physics and Ministry of Research and Innovation and Institute of Atomic Physics, Romania; Joint Institute for Nuclear Research (JINR), Ministry of Education and Science of the Russian Federation, National Research Centre Kurchatov Institute, Russian Science Foundation and Russian Foundation for Basic Research, Russia; Ministry of Education, Science, Research and Sport of the Slovak Republic, Slovakia; National Research Foundation of South Africa, South Africa; Swedish Research Council (VR) and Knut & Alice Wallenberg Foundation (KAW), Sweden; European Organization for Nuclear Research, Switzerland; Suranaree University of Technology (SUT), National Science and Technology Development Agency (NSDTA) and Office of the Higher Education Commission under NRU project of Thailand, Thailand; Turkish Energy, Nuclear and Mineral Research Agency (TENMAK), Turkey; National Academy of Sciences of Ukraine, Ukraine; Science and Technology Facilities Council (STFC), United Kingdom; National Science Foundation of the United States of America (NSF) and United States Department of Energy, Office of Nuclear Physics (DOE NP), United States of America.

[1] E. Shuryak, Strongly coupled quark-gluon plasma in heavy ion collisions, Rev. Mod. Phys. **89**, 035001 (2017).

[2] A. Andronic, P. Braun-Munzinger, K. Redlich, and J. Stachel, Decoding the phase structure of QCD via particle production at high energy, Nature (London) **561**, 321 (2018).

[3] M. Gyulassy and L. McLerran, New forms of QCD matter discovered at RHIC, Nucl. Phys. A **750**, 30 (2005).

[4] E. Shuryak, Physics of strongly coupled quark-gluon plasma, Prog. Part. Nucl. Phys. **62**, 48 (2009).

[5] P. Braun-Munzinger, V. Koch, T. Schäfer, and J. Stachel, Properties of hot and dense matter from relativistic heavy ion collisions, Phys. Rep. **621**, 76 (2016).

[6] J. Adams *et al.* (STAR Collaboration), Experimental and theoretical challenges in the search for the quark gluon plasma: The STAR Collaboration's critical assessment of the evidence from RHIC collisions, Nucl. Phys. A **757**, 102 (2005).

[7] M. Tanabashi *et al.* (Particle Data Group Collaboration), Review of Particle Physics, Phys. Rev. D **98**, 030001 (2018).

[8] G. Torrieri and J. Rafelski, Strange hadron resonances as a signature of freezeout dynamics, Phys. Lett. B **509**, 239 (2001).

[9] C. Adler *et al.* (STAR Collaboration), $K^*(892)^0$ production in relativistic heavy ion collisions at $\sqrt{s_{NN}} = 130$-GeV, Phys. Rev. C **66**, 061901 (2002).

[10] J. Adams *et al.* (STAR Collaboration), $K(892)^*$ resonance production in Au+Au and p+p collisions at $\sqrt{s_{NN}} = 200$ GeV at STAR, Phys. Rev. C **71**, 064902 (2005).

[11] C. Alt *et al.* (NA49 Collaboration), Energy dependence of $\phi$ meson production in central Pb+Pb collisions at $\sqrt{s_{NN}} = 6$ to 17 GeV, Phys. Rev. C **78**, 044907 (2008).

[12] B. I. Abelev *et al.* (STAR Collaboration), Energy and system size dependence of $\phi$ meson production in Cu+Cu and Au+Au collisions, Phys. Lett. B **673**, 183 (2009).

[13] B. I. Abelev *et al.* (STAR Collaboration), Measurements of $\phi$ meson production in relativistic heavy-ion collisions at RHIC, Phys. Rev. C **79**, 064903 (2009).

[14] M. M. Aggarwal *et al.* (STAR Collaboration), $K^{*0}$ production in Cu+Cu and Au+Au collisions at $\sqrt{s_{NN}} = 62.4$ GeV and 200 GeV, Phys. Rev. C **84**, 034909 (2011).

[15] A. Adare *et al.* (PHENIX Collaboration), Nuclear modification factors of $\phi$ mesons in $d + $ Au, Cu+Cu and Au+Au collisions at $\sqrt{s_{NN}} = 200$ GeV, Phys. Rev. C **83**, 024909 (2011).

[16] T. Anticic *et al.* (NA49 Collaboration), $K^*(892)^0$ and $\bar{K}^*(892)^0$ production in central Pb+Pb, Si+Si, C+C, and inelastic p+p collisions at 158*A* GeV, Phys. Rev. C **84**, 064909 (2011).

[17] A. Adare *et al.* (PHENIX Collaboration), Measurement of $K^0_S$ and $K^{*0}$ in p+p, d+Au, and Cu+Cu collisions at $\sqrt{s_{NN}} = 200$ GeV, Phys. Rev. C **90**, 054905 (2014).

[18] B. B. Abelev *et al.* (ALICE Collaboration), $K^*(892)^0$ and $\phi(1020)$ production in Pb–Pb collisions at $\sqrt{s_{NN}} = 2.76$ TeV, Phys. Rev. C **91**, 024609 (2015).

[19] L. Adamczyk *et al.* (STAR Collaboration), Probing parton dynamics of QCD matter with $\Omega$ and $\phi$ production, Phys. Rev. C **93**, 021903 (2016).

[20] A. G. Knospe, C. Markert, K. Werner, J. Steinheimer, and M. Bleicher, Hadronic resonance production and interaction in partonic and hadronic matter in the EPOS3 model with and without the hadronic afterburner UrQMD, Phys. Rev. C **93**, 014911 (2016).

[21] J. Adam *et al.* (ALICE Collaboration), $K^*(892)^0$ and $\phi(1020)$ meson production at high transverse momentum in pp and Pb–Pb collisions at $\sqrt{s_{NN}} = 2.76$ TeV, Phys. Rev. C **95**, 064606 (2017).

[22] S. Acharya *et al.* (ALICE Collaboration), Evidence of rescattering effect in Pb–Pb collisions at the LHC through production of $K^*(892)^0$ and $\phi(1020)$ mesons, Phys. Lett. B **802**, 135225 (2020).

[23] J. Adam *et al.* (ALICE Collaboration), Enhanced production of multi-strange hadrons in high-multiplicity proton-proton collisions, Nat. Phys. **13**, 535 (2017).

[24] V. Greco, C. M. Ko, and P. Levai, Parton Coalescence and the Anti-Proton/Pion Anomaly at RHIC, Phys. Rev. Lett. **90**, 202302 (2003).

[25] R. J. Fries, B. Muller, C. Nonaka, and S. A. Bass, Hadronization in Heavy Ion Collisions: Recombination and Fragmentation of Partons, Phys. Rev. Lett. **90**, 202303 (2003).

[26] B. I. Abelev *et al.* (STAR Collaboration), Energy dependence of $\pi^{\pm}$, $p$, and $\bar{p}$ transverse momentum spectra for Au+Au collisions at $\sqrt{s_{NN}} = 62.4$ and 200 GeV, Phys. Lett. B **655**, 104 (2007).

[27] S. Acharya *et al.* (ALICE Collaboration), Production of charged pions, kaons, and (anti-)protons in Pb–Pb and inelastic pp collisions at $\sqrt{s_{\rm NN}} = 5.02$ TeV, Phys. Rev. C **101**, 044907 (2020).

[28] B. B. Abelev *et al.* (ALICE Collaboration), Production of charged pions, kaons, and protons at large transverse momenta in $pp$ and Pb–Pb collisions at $\sqrt{s_{NN}} = 2.76$ TeV, Phys. Lett. B **736**, 196 (2014).

[29] B. B. Abelev *et al.* (ALICE Collaboration), $K^0_S$ and $\Lambda$ Production in Pb–Pb Collisions at $\sqrt{s_{NN}} = 2.76$ TeV, Phys. Rev. Lett. **111**, 222301 (2013).

[30] K. Aamodt *et al.* (ALICE Collaboration), Suppression of charged particle production at large transverse momentum in central Pb–Pb collisions at $\sqrt{s_{NN}} = 2.76$ TeV, Phys. Lett. B **696**, 30 (2011).

[31] J. Adam *et al.* (ALICE Collaboration), Centrality dependence of the nuclear modification factor of charged pions, kaons, and protons in Pb–Pb collisions at $\sqrt{s_{NN}} = 2.76$ TeV, Phys. Rev. C **93**, 034913 (2016).

[32] S. Chatrchyan *et al.* (CMS Collaboration), Study of high-$p_{\rm T}$ charged particle suppression in Pb–Pb compared to $pp$ collisions at $\sqrt{s_{NN}} = 2.76$ TeV, Eur. Phys. J. C **72**, 1945 (2012).

[33] G. Aad *et al.* (ATLAS Collaboration), Measurement of charged-particle spectra in Pb+Pb collisions at $\sqrt{s_{NN}} = 2.76$ TeV with the ATLAS detector at the LHC, J. High Energy Phys. 09 (2015) 050.

[34] J. Adams *et al.* (STAR Collaboration), Transverse Momentum and Collision Energy Dependence of High $p_{\rm T}$ Hadron Suppression in Au+Au Collisions at Ultrarelativistic Energies, Phys. Rev. Lett. **91**, 172302 (2003).

[35] B. I. Abelev *et al.* (STAR Collaboration), Identified Baryon and Meson Distributions at Large Transverse Momenta from Au+Au Collisions at $\sqrt{s_{NN}} = 200$ GeV, Phys. Rev. Lett. **97**, 152301 (2006).

[36] S. S. Adler *et al.* (PHENIX Collaboration), Suppressed $\pi^0$ Production at Large Transverse Momentum in Central Au+ Au Collisions at $\sqrt{s_{NN}} = 200$ GeV, Phys. Rev. Lett. **91**, 072301 (2003).

[37] J. Rafelski, J. Letessier, and G. Torrieri, Strange hadrons and their resonances: A diagnostic tool of QGP freezeout dynamics, Phys. Rev. C **64**, 054907 (2001); **65**, 069902(E) (2002).

[38] G.-Y. Qin and X.-N. Wang, Jet quenching in high-energy heavy-ion collisions, Int. J. Mod. Phys. E **24**, 1530014 (2015).

[39] J. Stachel, A. Andronic, P. Braun-Munzinger, and K. Redlich, Confronting LHC data with the statistical hadronization model, J. Phys.: Conf. Ser. **509**, 012019 (2014).

[40] E. Schnedermann, J. Sollfrank, and U. W. Heinz, Thermal phenomenology of hadrons from 200 AGeV S+S collisions, Phys. Rev. C **48**, 2462 (1993).

[41] B. Abelev *et al.* (ALICE Collaboration), Centrality dependence of $\pi$, K, and p production in Pb–Pb collisions at $\sqrt{s_{NN}} = 2.76$ TeV, Phys. Rev. C **88**, 044910 (2013).

[42] K. Aamodt *et al.* (ALICE Collaboration), Two-pion Bose-Einstein correlations in central Pb-Pb collisions at $\sqrt{s_{NN}} = 2.76$ TeV, Phys. Lett. B **696**, 328 (2011).

[43] M. L. Miller, K. Reygers, S. J. Sanders, and P. Steinberg, Glauber modeling in high energy nuclear collisions, Annu. Rev. Nucl. Part. Sci. **57**, 205 (2007).

[44] C. Loizides, J. Kamin, and D. d'Enterria, Improved Monte Carlo Glauber predictions at present and future nuclear colliders, Phys. Rev. C **97**, 054910 (2018); Phys. Rev.C **99**, 019901 (2019).

[45] B. Abelev *et al.* (ALICE Collaboration), Centrality determination of Pb–Pb collisions at $\sqrt{s_{NN}} = 2.76$ TeV with ALICE, Phys. Rev. C **88**, 044909 (2013).

[46] K. Aamodt *et al.* (ALICE Collaboration), The ALICE experiment at the CERN LHC, JINST **3**, S08002 (2008).

[47] B. B. Abelev *et al.* (ALICE Collaboration), Performance of the ALICE Experiment at the CERN LHC, Int. J. Mod. Phys. A **29**, 1430044 (2014).

[48] J. Adam *et al.* (ALICE Collaboration), Centrality Dependence of the Charged-Particle Multiplicity Density at Midrapidity in Pb–Pb Collisions at $\sqrt{s_{NN}} = 5.02$ TeV, Phys. Rev. Lett. **116**, 222302 (2016).

[49] B. Abelev *et al.* (ALICE Collaboration), Production of $K^*(892)^0$ and $\phi(1020)$ in pp collisions at $\sqrt{s} = 7$ TeV, Eur. Phys. J. C **72**, 2183 (2012).

[50] S. Acharya *et al.* (ALICE Collaboration), Multiplicity dependence of light-flavor hadron production in pp collisions at $\sqrt{s} = 7$ TeV, Phys. Rev. C **99**, 024906 (2019).

[51] J. Adam *et al.* (ALICE Collaboration), Production of $K^*(892)^0$ and $\phi(1020)$ in p–Pb collisions at $\sqrt{s_{NN}} = 5.02$ TeV, Eur. Phys. J. C **76**, 245 (2016).

[52] P. Skands, S. Carrazza, and J. Rojo, Tuning PYTHIA 8.1: the Monash 2013 Tune, Eur. Phys. J. C **74**, 3024 (2014).

[53] X.-N. Wang and M. Gyulassy, HIJING: A Monte Carlo model for multiple jet production in $pp$, $pA$, and $AA$ collisions, Phys. Rev. D **44**, 3501 (1991).

[54] R. Brun, F. Bruyant, F. Carminati, S. Giani, M. Maire, A. McPherson, G. Patrick, and L. Urban, GEANT: Detector Description and Simulation Tool; Oct 1994, CERN Program Library. CERN, Geneva, 1993, http://cds.cern.ch/record/1082634, Long Writeup W5013.

[55] S. Acharya *et al.* (ALICE Collaboration), Multiplicity dependence of $K^*(892)^0$ and $\phi(1020)$ production in pp collisions at $\sqrt{s} = 13$ TeV, Phys. Lett. B **807**, 135501 (2020).

[56] ALICE Collaboration, ALICE luminosity determination for pp collisions at $\sqrt{s} = 5$ TeV, https://cds.cern.ch/record/2202638.

[57] S. Acharya *et al.* (ALICE Collaboration), $K^*(892)^0$ and $\phi(1020)$ production at midrapidity in pp collisions at $\sqrt{s} = 8$ TeV, Phys. Rev. C **102**, 024912 (2020).

[58] S. Acharya *et al.* (ALICE Collaboration), Production of light-flavor hadrons in pp collisions at $\sqrt{s} = 7$ and $\sqrt{s} = 13$ TeV, Eur. Phys. J. C **81**, 256 (2021).

[59] K. Aamodt *et al.* (ALICE Collaboration), Midrapidity Antiproton-To-Proton Ratio in pp Collisions at $\sqrt{s} = 0.9$ and 7 TeV Measured by the ALICE Experiment, Phys. Rev. Lett. **105**, 072002 (2010).

[60] S. Agostinelli *et al.* (GEANT4 Collaboration), GEANT4–a simulation toolkit, Nucl. Instrum. Meth. A **506**, 250 (2003).

[61] G. Battistoni, S. Muraro, P. R. Sala, F. Cerutti, A. Ferrari, S. Roesler, A. Fasso, and J. Ranft, The FLUKA code: Description and benchmarking, AIP Conf. Proc. **896**, 31 (2007).

[62] T. Sjostrand, S. Mrenna, and P. Z. Skands, PYTHIA 6.4 Physics and Manual, J. High Energy Phys. 05 (2006) 026.

[63] P. Z. Skands, Tuning Monte Carlo generators: The Perugia tunes, Phys. Rev. D **82**, 074018 (2010).

[64] T. Sjőstrand, S. Mrenna, and P. Z. Skands, A Brief Introduction to PYTHIA 8.1, Comput. Phys. Commun. **178**, 852 (2008).

[65] C. Bierlich, Rope hadronization and strange particle production, EPJ Web Conf. **171**, 14003 (2018).

[66] T. Pierog, I. Karpenko, J. M. Katzy, E. Yatsenko, and K. Werner, EPOS LHC: Test of collective hadronization with data measured at the CERN Large Hadron Collider, Phys. Rev. C **92**, 034906 (2015).

[67] M. Bahr *et al.*, Herwig + + Physics and Manual, Eur. Phys. J. C **58**, 639 (2008).

[68] C. Tsallis, Possible Generalization of Boltzmann-Gibbs Statistics, J. Statist. Phys. **52**, 479 (1988).

[69] B. Andersson, G. Gustafson, G. Ingelman, and T. Sjostrand, Parton fragmentation and string dynamics, Phys. Rep. **97**, 31 (1983).

[70] B. I. Abelev *et al.* (STAR Collaboration), Hadronic resonance production in d+Au collisions at $\sqrt{s_{NN}} = 200$ GeV at RHIC, Phys. Rev. C **78**, 044906 (2008).

[71] S. A. Bass *et al.*, Microscopic models for ultrarelativistic heavy ion collisions, Prog. Part. Nucl. Phys. **41**, 255 (1998).

[72] M. Bleicher *et al.*, Relativistic hadron hadron collisions in the ultrarelativistic quantum molecular dynamics model, J. Phys. G **25**, 1859 (1999).

[73] A. Adare *et al.* (PHENIX Collaboration), Neutral pion production with respect to centrality and reaction plane in Au+Au collisions at $\sqrt{s_{NN}}$=200 GeV, Phys. Rev. C **87**, 034911 (2013).

[74] P. Christiansen, K. Tywoniuk, and V. Vislavicius, Universal scaling dependence of QCD energy loss from data driven studies, Phys. Rev. C **89**, 034912 (2014).

[75] A. Ortiz and O. Vázquez, Energy density and path-length dependence of the fractional momentum loss in heavy-ion collisions at $\sqrt{s_{NN}}$ from 62.4 to 5020 GeV, Phys. Rev. C **97**, 014910 (2018).

[76] S. Acharya *et al.* (ALICE Collaboration), Transverse momentum spectra and nuclear modification factors of charged particles in Xe–Xe collisions at $\sqrt{s_{NN}} = 5.44$ TeV, Phys. Lett. B **788**, 166 (2019).



S. Acharya,[143] D. Adamová,[98] A. Adler,[76] J. Adolfsson,[83] G. Aglieri Rinella,[35] M. Agnello,[31] N. Agrawal,[55] Z. Ahammed,[143] S. Ahmad,[16] S. U. Ahn,[78] I. Ahuja,[39] Z. Akbar,[52] A. Akindinov,[95] M. Al-Turany,[110] S. N. Alam,[41] D. Aleksandrov,[91] B. Alessandro,[61] H. M. Alfanda,[7] R. Alfaro Molina,[73] B. Ali,[16] Y. Ali,[14] A. Alici,[26] N. Alizadehvandchali,[127] A. Alkin,[35]

J. Alme,[21] T. Alt,[70] L. Altenkamper,[21] I. Altsybeev,[115] M. N. Anaam,[7] C. Andrei,[49] D. Andreou,[93] A. Andronic,[146] M. Angeletti,[35] V. Anguelov,[107] F. Antinori,[58] P. Antonioli,[55] C. Anuj,[16] N. Apadula,[82] L. Aphecetche,[117] H. Appelshäuser,[70] S. Arcelli,[26] R. Arnaldi,[61] I. C. Arsene,[20] M. Arslandok,[148,107] A. Augustinus,[35] R. Averbeck,[110] S. Aziz,[80] M. D. Azmi,[16] A. Badalà,[57] Y. W. Baek,[42] X. Bai,[131,110] R. Bailhache,[70] Y. Bailung,[51] R. Bala,[104] A. Balbino,[31] A. Baldisseri,[140] B. Balis,[2] M. Ball,[44] D. Banerjee,[4] R. Barbera,[27] L. Barioglio,[108,25] M. Barlou,[87] G. G. Barnaföldi,[147] L. S. Barnby,[97] V. Barret,[137] C. Bartels,[130] K. Barth,[35] E. Bartsch,[70] F. Baruffaldi,[28] N. Bastid,[137] S. Basu,[83] G. Batigne,[117] B. Batyunya,[77] D. Bauri,[50] J. L. Bazo Alba,[114] I. G. Bearden,[92] C. Beattie,[148] I. Belikov,[139] A. D. C. Bell Hechavarria,[146] F. Bellini,[26,35] R. Bellwied,[127] S. Belokurova,[115] V. Belyaev,[96] G. Bencedi,[71] S. Beole,[25] A. Bercuci,[49] Y. Berdnikov,[101] A. Berdnikova,[107] D. Berenyi,[147] L. Bergmann,[107] M. G. Besoiu,[69] L. Betev,[35] P. P. Bhaduri,[143] A. Bhasin,[104] I. R. Bhat,[104] M. A. Bhat,[4] B. Bhattacharjee,[43] P. Bhattacharya,[23] L. Bianchi,[25] N. Bianchi,[53] J. Bielčík,[38] J. Bielčíková,[98] J. Biernat,[120] A. Bilandzic,[108] G. Biro,[147] S. Biswas,[4] J. T. Blair,[121] D. Blau,[91] M. B. Blidaru,[110] C. Blume,[70] G. Boca,[29,59] F. Bock,[99] A. Bogdanov,[96] S. Boi,[23] J. Bok,[63] L. Boldizsár,[147] A. Bolozdynya,[96] M. Bombara,[39] P. M. Bond,[35] G. Bonomi,[142,59] H. Borel,[140] A. Borissov,[84] H. Bossi,[148] E. Botta,[25] L. Bratrud,[70] P. Braun-Munzinger,[110] M. Bregant,[123] M. Broz,[38] G. E. Bruno,[109,34] M. D. Buckland,[130] D. Budnikov,[111] H. Buesching,[70] S. Bufalino,[31] O. Bugnon,[117] P. Buhler,[116] Z. Buthelezi,[74,134] J.B. Butt,[14] S.A. Bysiak,[120] D. Caffarri,[93] M. Cai,[28,7] H. Caines,[148] A. Caliva,[110] E. Calvo Villar,[114] J. M. M. Camacho,[122] R.S. Camacho,[46] P. Camerini,[24] F. D. M. Canedo,[123] F. Carnesecchi,[35,26] R. Caron,[140] J. Castillo Castellanos,[140] E. A. R. Casula,[23] F. Catalano,[31] C. Ceballos Sanchez,[77] P. Chakraborty,[50] S. Chandra,[143] S. Chapeland,[35] M. Chartier,[130] S. Chattopadhyay,[143] S. Chattopadhyay,[112] A. Chauvin,[23] T. G. Chavez,[46] C. Cheshkov,[138] B. Cheynis,[138] V. Chibante Barroso,[35] D. D. Chinellato,[124] S. Cho,[63] P. Chochula,[35] P. Christakoglou,[93] C. H. Christensen,[92] P. Christiansen,[83] T. Chujo,[136] C. Cicalo,[56] L. Cifarelli,[26] F. Cindolo,[55] M. R. Ciupek,[110] G. Clai,[55,a] J. Cleymans,[126,b] F. Colamaria,[54] J. S. Colburn,[113] D. Colella,[109,54,34,147] A. Collu,[82] M. Colocci,[35,26] M. Concas,[61,c] G. Conesa Balbastre,[81] Z. Conesa del Valle,[80] G. Contin,[24] J.G. Contreras,[38] M. L. Coquet,[140] T.M. Cormier,[99] P. Cortese,[32] M. R. Cosentino,[125] F. Costa,[35] S. Costanza,[29,59] P. Crochet,[137] E. Cuautle,[71] P. Cui,[7] L. Cunqueiro,[99] A. Dainese,[58] F. P. A. Damas,[117,140] M. C. Danisch,[107] A. Danu,[69] I. Das,[112] P. Das,[89] P. Das,[4] S. Das,[4] A. Dash,[89] S. Dash,[50] S. De,[89] A. De Caro,[30] G. de Cataldo,[54] L. De Cilladi,[25] J. de Cuveland,[40] A. De Falco,[23] D. De Gruttola,[30] N. De Marco,[61] C. De Martin,[24] S. De Pasquale,[30] S. Deb,[51] H. F. Degenhardt,[123] K. R. Deja,[144] L. Dello Stritto,[30] S. Delsanto,[25] W. Deng,[7] P. Dhankher,[19] D. Di Bari,[34] A. Di Mauro,[35] R. A. Diaz,[8] T. Dietel,[126] Y. Ding,[138,7] R. Divià,[35] D.U. Dixit,[19] Ø. Djuvsland,[21] U. Dmitrieva,[65] J. Do,[63] A. Dobrin,[69] B. Dönigus,[70] O. Dordic,[20] A. K. Dubey,[143] A. Dubla,[110,93] S. Dudi,[103] M. Dukhishyam,[89] P. Dupieux,[137] N. Dzalaiova,[13] T. M. Eder,[146] R. J. Ehlers,[99] V. N. Eikeland,[21] D. Elia,[54] B. Erazmus,[117] F. Ercolessi,[26] F. Erhardt,[102] A. Erokhin,[115] M. R. Ersdal,[21] B. Espagnon,[80] G. Eulisse,[35] D. Evans,[113] S. Evdokimov,[94] L. Fabbietti,[108] M. Faggin,[28] J. Faivre,[81] F. Fan,[7] A. Fantoni,[53] M. Fasel,[99] P. Fecchio,[31] A. Feliciello,[61] G. Feofilov,[115] A. Fernández Téllez,[46] A. Ferrero,[140] A. Ferretti,[25] V. J. G. Feuillard,[107] J. Figiel,[120] S. Filchagin,[111] D. Finogeev,[65] F. M. Fionda,[56,21] G. Fiorenza,[35,109] F. Flor,[127] A. N. Flores,[121] S. Foertsch,[74] P. Foka,[110] S. Fokin,[91] E. Fragiacomo,[62] E. Frajna,[147] U. Fuchs,[35] N. Funicello,[30] C. Furget,[81] A. Furs,[65] J. J. Gaardhøje,[92] M. Gagliardi,[25] A. M. Gago,[114] A. Gal,[139] C. D. Galvan,[122] P. Ganoti,[87] C. Garabatos,[110] J. R. A. Garcia,[46] E. Garcia-Solis,[10] K. Garg,[117] C. Gargiulo,[35] A. Garibli,[90] K. Garner,[146] P. Gasik,[110] E. F. Gauger,[121] A. Gautam,[129] M. B. Gay Ducati,[72] M. Germain,[117] J. Ghosh,[112] P. Ghosh,[143] S. K. Ghosh,[4] M. Giacalone,[26] P. Gianotti,[53] P. Giubellino,[110,61] P. Giubilato,[28] A. M. C. Glaenzer,[140] P. Glässel,[107] D. J. Q. Goh,[85] V. Gonzalez,[145] L. H. González-Trueba,[73] S. Gorbunov,[40] M.B. Gorgon,[2] L. Görlich,[120] S. Gotovac,[36] V. Grabski,[73] L. K. Graczykowski,[144] L. Greiner,[82] A. Grelli,[64] C. Grigoras,[35] V. Grigoriev,[96] A. Grigoryan,[1,b] S. Grigoryan,[77,1] O. S. Groettvik,[21] F. Grosa,[35,61] J. F. Grosse-Oetringhaus,[35] R. Grosso,[110] G. G. Guardiano,[124] R. Guernane,[81] M. Guilbaud,[117] K. Gulbrandsen,[92] T. Gunji,[135] A. Gupta,[104] R. Gupta,[104] I. B. Guzman,[46] S.P. Guzman,[46] L. Gyulai,[147] M. K. Habib,[110] C. Hadjidakis,[80] G. Halimoglu,[70] H. Hamagaki,[85] G. Hamar,[147] M. Hamid,[7] R. Hannigan,[121] M. R. Haque,[144,89] A. Harlenderova,[110] J. W. Harris,[148] A. Harton,[10] J. A. Hasenbichler,[35] H. Hassan,[99] D. Hatzifotiadou,[55] P. Hauer,[44] L.B. Havener,[148] S. Hayashi,[135] S. T. Heckel,[108] E. Hellbär,[70] H. Helstrup,[37] T. Herman,[38] E. G. Hernandez,[46] G. Herrera Corral,[9] F. Herrmann,[146] K. F. Hetland,[37] H. Hillemanns,[35] C. Hills,[130] B. Hippolyte,[139] B. Hofman,[64] B. Hohlweger,[93,108] J. Honermann,[146] G. H. Hong,[149] D. Horak,[38] S. Hornung,[110] A. Horzyk,[2] R. Hosokawa,[15] P. Hristov,[35] C. Huang,[80] C. Hughes,[133] P. Huhn,[70] T. J. Humanic,[100] H. Hushnud,[112] L. A. Husova,[146] D. Hutter,[40] J. P. Iddon,[35,130] R. Ilkaev,[111] H. Ilyas,[14] M. Inaba,[136] G.M. Innocenti,[35] M. Ippolitov,[91] A. Isakov,[38,98] M. S. Islam,[112] M. Ivanov,[110] V. Ivanov,[101] V. Izucheev,[94] M. Jablonski,[2] B. Jacak,[82] N. Jacazio,[35] P.M. Jacobs,[82] S. Jadlovska,[119] J. Jadlovsky,[119] S. Jaelani,[64] C. Jahnke,[124,123] M. J. Jakubowska,[144] M. A. Janik,[144] T. Janson,[76] C. Jena,[89] M. Jercic,[102] O. Jevons,[113] F. Jonas,[99,146] P.G. Jones,[113] J. M. Jowett,[35,110] J. Jung,[70] M. Jung,[70] A. Junique,[35] A. Jusko,[113] J. Kaewjai,[118] P. Kalinak,[66] A. Kalweit,[35] V. Kaplin,[96] S. Kar,[7] A. Karasu Uysal,[79] D. Karatovic,[102] O. Karavichev,[65] T. Karavicheva,[65] P. Karczmarczyk,[144] E. Karpechev,[65] A. Kazantsev,[91] U. Kebschull,[76] R. Keidel,[48] D. L. D. Keijdener,[64] M. Keil,[35] B. Ketzer,[44] Z. Khabanova,[93] A. M. Khan,[7] S. Khan,[16] A. Khanzadeev,[101] Y. Kharlov,[94] A. Khatun,[16] A. Khuntia,[120] B. Kileng,[37] B. Kim,[17,63] D. Kim,[149] D. J. Kim,[128] E. J. Kim,[75] J. Kim,[149] J. S. Kim,[42] J. Kim,[107] J. Kim,[149] J. Kim,[75] M. Kim,[107] S. Kim,[18] T. Kim,[149] S. Kirsch,[70] I. Kisel,[40] S. Kiselev,[95] A. Kisiel,[144] J. P. Kitowski,[2] J. L. Klay,[6] J. Klein,[35] S. Klein,[82] C. Klein-Bösing,[146] M. Kleiner,[70] T. Klemenz,[108] A. Kluge,[35] A. G. Knospe,[127] C. Kobdaj,[118] M. K. Köhler,[107] T. Kollegger,[110] A. Kondratyev,[77] N. Kondratyeva,[96] E. Kondratyuk,[94] J. Konig,[70] S. A. Konigstorfer,[108] P. J. Konopka,[35,2] G. Kornakov,[144] S. D. Koryciak,[2] L. Koska,[119] A. Kotliarov,[98] O. Kovalenko,[88] V. Kovalenko,[115] M. Kowalski,[120] I. Králik,[66] A. Kravčáková,[39]

L. Kreis,[110] M. Krivda,[113,66] F. Krizek,[98] K. Krizkova Gajdosova,[38] M. Kroesen,[107] M. Krüger,[70] E. Kryshen,[101] M. Krzewicki,[40] V. Kučera,[35] C. Kuhn,[139] P. G. Kuijer,[93] T. Kumaoka,[136] D. Kumar,[143] L. Kumar,[103] N. Kumar,[103] S. Kundu,[35,89] P. Kurashvili,[88] A. Kurepin,[65] A. B. Kurepin,[65] A. Kuryakin,[111] S. Kushpil,[98] J. Kvapil,[113] M. J. Kweon,[63] J. Y. Kwon,[63] Y. Kwon,[149] S. L. La Pointe,[40] P. La Rocca,[27] Y. S. Lai,[82] A. Lakrathok,[118] M. Lamanna,[35] R. Langoy,[132] K. Lapidus,[35] P. Larionov,[53] E. Laudi,[35] L. Lautner,[35,108] R. Lavicka,[38] T. Lazareva,[115] R. Lea,[142,24,59] J. Lee,[136] J. Lehrbach,[40] R. C. Lemmon,[97] I. León Monzón,[122] E. D. Lesser,[19] M. Lettrich,[35,108] P. Lévai,[147] X. Li,[11] X. L. Li,[7] J. Lien,[132] R. Lietava,[113] B. Lim,[17] S. H. Lim,[17] V. Lindenstruth,[40] A. Lindner,[49] C. Lippmann,[110] A. Liu,[19] J. Liu,[130] I. M. Lofnes,[21] V. Loginov,[96] C. Loizides,[99] P. Loncar,[36] J. A. Lopez,[107] X. Lopez,[137] E. López Torres,[8] J.R. Luhder,[146] M. Lunardon,[28] G. Luparello,[62] Y. G. Ma,[41] A. Maevskaya,[65] M. Mager,[35] T. Mahmoud,[44] A. Maire,[139] M. Malaev,[101] Q. W. Malik,[20] L. Malinina,[77,d] D. Mal'Kevich,[95] N. Mallick,[51] P. Malzacher,[110] G. Mandaglio,[33,57] V. Manko,[91] F. Manso,[137] V. Manzari,[54] Y. Mao,[7] J. Mareš,[68] G. V. Margagliotti,[24] A. Margotti,[55] A. Marín,[110] C. Markert,[121] M. Marquard,[70] N. A. Martin,[107] P. Martinengo,[35] J. L. Martinez,[127] M. I. Martínez,[46] G. Martínez García,[117] S. Masciocchi,[110] M. Masera,[25] A. Masoni,[56] L. Massacrier,[80] A. Mastroserio,[141,54] A. M. Mathis,[108] O. Matonoha,[83] P. F. T. Matuoka,[123] A. Matyja,[120] C. Mayer,[120] A.L. Mazuecos,[35] F. Mazzaschi,[25] M. Mazzilli,[35] M.A. Mazzoni,[60] J. E. Mdhluli,[134] A. F. Mechler,[70] F. Meddi,[22] Y. Melikyan,[65] A. Menchaca-Rocha,[73] E. Meninno,[116,30] A. S. Menon,[127] M. Meres,[13] S. Mhlanga,[126,74] Y. Miake,[136] L. Micheletti,[61,25] L. C. Migliorin,[138] D. L. Mihaylov,[108] K. Mikhaylov,[77,95] A. N. Mishra,[147] D. Miśkowiec,[110] A. Modak,[4] A. P. Mohanty,[64] B. Mohanty,[89] M. Mohisin Khan,[16] Z. Moravcova,[92] C. Mordasini,[108] D. A. Moreira De Godoy,[146] L. A. P. Moreno,[46] I. Morozov,[65] A. Morsch,[35] T. Mrnjavac,[35] V. Muccifora,[53] E. Mudnic,[36] D. Mühlheim,[146] S. Muhuri,[143] J. D. Mulligan,[82] A. Mulliri,[23] M. G. Munhoz,[123] R. H. Munzer,[70] H. Murakami,[135] S. Murray,[126] L. Musa,[35] J. Musinsky,[66] C. J. Myers,[127] J. W. Myrcha,[144] B. Naik,[50] R. Nair,[88] B.K. Nandi,[50] R. Nania,[55] E. Nappi,[54] M. U. Naru,[14] A.F. Nassirpour,[83] A. Nath,[107] C. Nattrass,[133] A. Neagu,[20] L. Nellen,[71] S. V. Nesbo,[37] G. Neskovic,[40] D. Nesterov,[115] B. S. Nielsen,[92] S. Nikolaev,[91] S. Nikulin,[91] V. Nikulin,[101] F. Noferini,[55] S. Noh,[12] P. Nomokonov,[77] J. Norman,[130] N. Novitzky,[136] P. Nowakowski,[144] A. Nyanin,[91] J. Nystrand,[21] M. Ogino,[85] A. Ohlson,[83] V. A. Okorokov,[96] J. Oleniacz,[144] A. C. Oliveira Da Silva,[133] M. H. Oliver,[148] A. Onnerstad,[128] C. Oppedisano,[61] A. Ortiz Velasquez,[71] T. Osako,[47] A. Oskarsson,[83] J. Otwinowski,[120] K. Oyama,[85] Y. Pachmayer,[107] S. Padhan,[50] D. Pagano,[142,59] G. Paić,[71] A. Palasciano,[54] J. Pan,[145] S. Panebianco,[140] P. Pareek,[143] J. Park,[63] J. E. Parkkila,[128] S. P. Pathak,[127] R. N. Patra,[104,35] B. Paul,[23] J. Pazzini,[142,59] H. Pei,[7] T. Peitzmann,[64] X. Peng,[7] L. G. Pereira,[72] H. Pereira Da Costa,[140] D. Peresunko,[91] G. M. Perez,[8] S. Perrin,[140] Y. Pestov,[5] V. Petráček,[38] M. Petrovici,[49] R. P. Pezzi,[72] S. Piano,[62] M. Pikna,[13] P. Pillot,[117] O. Pinazza,[55,35] L. Pinsky,[127] C. Pinto,[27] S. Pisano,[53] M. Płoskoń,[82] M. Planinic,[102] F. Pliquett,[70] M. G. Poghosyan,[99] B. Polichtchouk,[94] S. Politano,[31] N. Poljak,[102] A. Pop,[49] S. Porteboeuf-Houssais,[137] J. Porter,[82] V. Pozdniakov,[77] S. K. Prasad,[4] R. Preghenella,[55] F. Prino,[61] C. A. Pruneau,[145] I. Pshenichnov,[65] M. Puccio,[35] S. Qiu,[93] L. Quaglia,[25] R. E. Quishpe,[127] S. Ragoni,[113] A. Rakotozafindrabe,[140] L. Ramello,[32] F. Rami,[139] S. A. R. Ramirez,[46] A. G. T. Ramos,[34] R. Raniwala,[105] S. Raniwala,[105] S. S. Räsänen,[45] R. Rath,[51] I. Ravasenga,[93] K. F. Read,[99,133] A. R. Redelbach,[40] K. Redlich,[88,e] A. Rehman,[21] P. Reichelt,[70] F. Reidt,[35] H. A. Reme-ness,[37] R. Renfordt,[70] Z. Rescakova,[39] K. Reygers,[107] A. Riabov,[101] V. Riabov,[101] T. Richert,[83,92] M. Richter,[20] W. Riegler,[35] F. Riggi,[27] C. Ristea,[69] S. P. Rode,[51] M. Rodríguez Cahuantzi,[46] K. Røed,[20] R. Rogalev,[94] E. Rogochaya,[77] T. S. Rogoschinski,[70] D. Rohr,[35] D. Röhrich,[21] P. F. Rojas,[46] P. S. Rokita,[144] F. Ronchetti,[53] A. Rosano,[33,57] E. D. Rosas,[71] A. Rossi,[58] A. Rotondi,[29,59] A. Roy,[51] P. Roy,[112] S. Roy,[50] N. Rubini,[26] O. V. Rueda,[83] R. Rui,[24] B. Rumyantsev,[77] P. G. Russek,[2] A. Rustamov,[90] E. Ryabinkin,[91] Y. Ryabov,[101] A. Rybicki,[120] H. Rytkonen,[128] W. Rzesa,[144] O. A. M. Saarimaki,[45] R. Sadek,[117] S. Sadovsky,[94] J. Saetre,[21] K. Šafařík,[38] S. K. Saha,[143] S. Saha,[89] B. Sahoo,[50] P. Sahoo,[50] R. Sahoo,[51] S. Sahoo,[67] D. Sahu,[51] P. K. Sahu,[67] J. Saini,[143] S. Sakai,[136] S. Sambyal,[104] V. Samsonov,[101,96,b] D. Sarkar,[145] N. Sarkar,[143] P. Sarma,[43] V. M. Sarti,[108] M. H. P. Sas,[148] J. Schambach,[99,121] H. S. Scheid,[70] C. Schiaua,[49] R. Schicker,[107] A. Schmah,[107] C. Schmidt,[110] H.R. Schmidt,[106] M.O. Schmidt,[107] M. Schmidt,[106] N.V. Schmidt,[99,70] A.R. Schmier,[133] R. Schotter,[139] J. Schukraft,[35] Y. Schutz,[139] K. Schwarz,[110] K. Schweda,[110] G. Scioli,[26] E. Scomparin,[61] J. E. Seger,[15] Y. Sekiguchi,[135] D. Sekihata,[135] I. Selyuzhenkov,[110,96] S. Senyukov,[139] J. J. Seo,[63] D. Serebryakov,[65] L. Šerkšnytė,[108] A. Sevcenco,[69] T. J. Shaba,[74] A. Shabanov,[65] A. Shabetai,[117] R. Shahoyan,[35] W. Shaikh,[112] A. Shangaraev,[94] A. Sharma,[103] H. Sharma,[120] M. Sharma,[104] N. Sharma,[103] S. Sharma,[104] O. Sheibani,[127] K. Shigaki,[47] M. Shimomura,[86] S. Shirinkin,[95] Q. Shou,[41] Y. Sibiriak,[91] S. Siddhanta,[56] T. Siemiarczuk,[88] T. F. Silva,[123] D. Silvermyr,[83] G. Simonetti,[35] B. Singh,[108] R. Singh,[89] R. Singh,[104] R. Singh,[51] V. K. Singh,[143] V. Singhal,[143] T. Sinha,[112] B. Sitar,[13] M. Sitta,[32] T. B. Skaali,[20] G. Skorodumovs,[107] M. Slupecki,[45] N. Smirnov,[148] R. J. M. Snellings,[64] C. Soncco,[114] J. Song,[127] A. Songmoolnak,[118] F. Soramel,[28] S. Sorensen,[133] I. Sputowska,[120] J. Stachel,[107] I. Stan,[69] P. J. Steffanic,[133] S. F. Stiefelmaier,[107] D. Stocco,[117] I. Storehaug,[20] M. M. Storetvedt,[37] C. P. Stylianidis,[93] A. A. P. Suaide,[123] T. Sugitate,[47] C. Suire,[80] M. Suljic,[35] R. Sultanov,[95] M. Šumbera,[98] V. Sumberia,[104] S. Sumowidagdo,[52] S. Swain,[67] A. Szabo,[13] I. Szarka,[13] U. Tabassam,[14] S. F. Taghavi,[108] G. Taillepied,[137] J. Takahashi,[124] G. J. Tambave,[21] S. Tang,[137,7] Z. Tang,[131] M. Tarhini,[117] M. G. Tarzila,[49] A. Tauro,[35] G. Tejeda Muñoz,[46] A. Telesca,[35] L. Terlizzi,[25] C. Terrevoli,[127] G. Tersimonov,[3] S. Thakur,[143] D. Thomas,[121] R. Tieulent,[138] A. Tikhonov,[65] A. R. Timmins,[127] M. Tkacik,[119] A. Toia,[70] N. Topilskaya,[65] M. Toppi,[53] F. Torales-Acosta,[19] T. Tork,[80] S. R. Torres,[38] A. Trifiró,[33,57] S. Tripathy,[55,71] T. Tripathy,[50] S. Trogolo,[35,28] G. Trombetta,[34] V. Trubnikov,[3] W. H. Trzaska,[128] T. P. Trzcinski,[144] B. A. Trzeciak,[38] A. Tumkin,[111] R. Turrisi,[58] T. S. Tveter,[20] K. Ullaland,[21] A. Uras,[138] M. Urioni,[59,142] G. L. Usai,[23] M. Vala,[39] N. Valle,[59,29] S. Vallero,[61] N. van der Kolk,[64] L. V. R. van Doremalen,[64] M. van Leeuwen,[93]

P. Vande Vyvre,[35] D. Varga,[147] Z. Varga,[147] M. Varga-Kofarago,[147] A. Vargas,[46] M. Vasileiou,[87] A. Vasiliev,[91] O. Vázquez Doce,[108] V. Vechernin,[115] E. Vercellin,[25] S. Vergara Limón,[46] L. Vermunt,[64] R. Vértesi,[147] M. Verweij,[64] L. Vickovic,[36] Z. Vilakazi,[134] O. Villalobos Baillie,[113] G. Vino,[54] A. Vinogradov,[91] T. Virgili,[30] V. Vislavicius,[92] A. Vodopyanov,[77] B. Volkel,[35] M. A. Völkl,[107] K. Voloshin,[95] S. A. Voloshin,[145] G. Volpe,[34] B. von Haller,[35] I. Vorobyev,[108] D. Voscek,[119] J. Vrláková,[39] B. Wagner,[21] C. Wang,[41] D. Wang,[41] M. Weber,[116] R. J. G. V. Weelden,[93] A. Wegrzynek,[35] S. C. Wenzel,[35] J. P. Wessels,[146] J. Wiechula,[70] J. Wikne,[20] G. Wilk,[88] J. Wilkinson,[110] G. A. Willems,[146] E. Willsher,[113] B. Windelband,[107] M. Winn,[140] W. E. Witt,[133] J. R. Wright,[121] W. Wu,[41] Y. Wu,[131] R. Xu,[7] S. Yalcin,[79] Y. Yamaguchi,[47] K. Yamakawa,[47] S. Yang,[21] S. Yano,[47,140] Z. Yin,[7] H. Yokoyama,[64] I.-K. Yoo,[17] J. H. Yoon,[63] S. Yuan,[21] A. Yuncu,[107] V. Zaccolo,[24] A. Zaman,[14] C. Zampolli,[35] H. J. C. Zanoli,[64] N. Zardoshti,[35] A. Zarochentsev,[115] P. Závada,[68] N. Zaviyalov,[111] H. Zbroszczyk,[144] M. Zhalov,[101] S. Zhang,[41] X. Zhang,[7] Y. Zhang,[131] V. Zherebchevskii,[115] Y. Zhi,[11] D. Zhou,[7] Y. Zhou,[92] J. Zhu,[7,110] Y. Zhu,[7] A. Zichichi,[26] G. Zinovjev,[3] and N. Zurlo[142,59]

(ALICE Collaboration)

[1]*A.I. Alikhanyan National Science Laboratory (Yerevan Physics Institute) Foundation, Yerevan, Armenia*
[2]*AGH University of Science and Technology, Cracow, Poland*
[3]*Bogolyubov Institute for Theoretical Physics, National Academy of Sciences of Ukraine, Kiev, Ukraine*
[4]*Bose Institute, Department of Physics and Centre for Astroparticle Physics and Space Science (CAPSS), Kolkata, India*
[5]*Budker Institute for Nuclear Physics, Novosibirsk, Russia*
[6]*California Polytechnic State University, San Luis Obispo, California, USA*
[7]*Central China Normal University, Wuhan, China*
[8]*Centro de Aplicaciones Tecnológicas y Desarrollo Nuclear (CEADEN), Havana, Cuba*
[9]*Centro de Investigación y de Estudios Avanzados (CINVESTAV), Mexico City and Mérida, Mexico*
[10]*Chicago State University, Chicago, Illinois, USA*
[11]*China Institute of Atomic Energy, Beijing, China*
[12]*Chungbuk National University, Cheongju, Republic of Korea*
[13]*Comenius University Bratislava, Faculty of Mathematics, Physics and Informatics, Bratislava, Slovakia*
[14]*COMSATS University Islamabad, Islamabad, Pakistan*
[15]*Creighton University, Omaha, Nebraska, USA*
[16]*Department of Physics, Aligarh Muslim University, Aligarh, India*
[17]*Department of Physics, Pusan National University, Pusan, Republic of Korea*
[18]*Department of Physics, Sejong University, Seoul, Republic of Korea*
[19]*Department of Physics, University of California, Berkeley, California, USA*
[20]*Department of Physics, University of Oslo, Oslo, Norway*
[21]*Department of Physics and Technology, University of Bergen, Bergen, Norway*
[22]*Dipartimento di Fisica dell'Università 'La Sapienza' and Sezione INFN, Rome, Italy*
[23]*Dipartimento di Fisica dell'Università and Sezione INFN, Cagliari, Italy*
[24]*Dipartimento di Fisica dell'Università and Sezione INFN, Trieste, Italy*
[25]*Dipartimento di Fisica dell'Università and Sezione INFN, Turin, Italy*
[26]*Dipartimento di Fisica e Astronomia dell'Università and Sezione INFN, Bologna, Italy*
[27]*Dipartimento di Fisica e Astronomia dell'Università and Sezione INFN, Catania, Italy*
[28]*Dipartimento di Fisica e Astronomia dell'Università and Sezione INFN, Padova, Italy*
[29]*Dipartimento di Fisica e Nucleare e Teorica, Università di Pavia, Pavia, Italy*
[30]*Dipartimento di Fisica 'E.R. Caianiello' dell'Università and Gruppo Collegato INFN, Salerno, Italy*
[31]*Dipartimento DISAT del Politecnico and Sezione INFN, Turin, Italy*
[32]*Dipartimento di Scienze e Innovazione Tecnologica dell'Università del Piemonte Orientale and INFN Sezione di Torino, Alessandria, Italy*
[33]*Dipartimento di Scienze MIFT, Università di Messina, Messina, Italy*
[34]*Dipartimento Interateneo di Fisica 'M. Merlin' and Sezione INFN, Bari, Italy*
[35]*European Organization for Nuclear Research (CERN), Geneva, Switzerland*
[36]*Faculty of Electrical Engineering, Mechanical Engineering and Naval Architecture, University of Split, Split, Croatia*
[37]*Faculty of Engineering and Science, Western Norway University of Applied Sciences, Bergen, Norway*
[38]*Faculty of Nuclear Sciences and Physical Engineering, Czech Technical University in Prague, Prague, Czech Republic*
[39]*Faculty of Science, P.J. Šafárik University, Košice, Slovakia*
[40]*Frankfurt Institute for Advanced Studies, Johann Wolfgang Goethe-Universität Frankfurt, Frankfurt, Germany*
[41]*Fudan University, Shanghai, China*
[42]*Gangneung-Wonju National University, Gangneung, Republic of Korea*
[43]*Gauhati University, Department of Physics, Guwahati, India*
[44]*Helmholtz-Institut für Strahlen- und Kernphysik, Rheinische Friedrich-Wilhelms-Universität Bonn, Bonn, Germany*

[45]*Helsinki Institute of Physics (HIP), Helsinki, Finland*
[46]*High Energy Physics Group, Universidad Autónoma de Puebla, Puebla, Mexico*
[47]*Hiroshima University, Hiroshima, Japan*
[48]*Hochschule Worms, Zentrum für Technologietransfer und Telekommunikation (ZTT), Worms, Germany*
[49]*Horia Hulubei National Institute of Physics and Nuclear Engineering, Bucharest, Romania*
[50]*Indian Institute of Technology Bombay (IIT), Mumbai, India*
[51]*Indian Institute of Technology Indore, Indore, India*
[52]*Indonesian Institute of Sciences, Jakarta, Indonesia*
[53]*INFN, Laboratori Nazionali di Frascati, Frascati, Italy*
[54]*INFN, Sezione di Bari, Bari, Italy*
[55]*INFN, Sezione di Bologna, Bologna, Italy*
[56]*INFN, Sezione di Cagliari, Cagliari, Italy*
[57]*INFN, Sezione di Catania, Catania, Italy*
[58]*INFN, Sezione di Padova, Padova, Italy*
[59]*INFN, Sezione di Pavia, Pavia, Italy*
[60]*INFN, Sezione di Roma, Rome, Italy*
[61]*INFN, Sezione di Torino, Turin, Italy*
[62]*INFN, Sezione di Trieste, Trieste, Italy*
[63]*Inha University, Incheon, Republic of Korea*
[64]*Institute for Gravitational and Subatomic Physics (GRASP), Utrecht University/Nikhef, Utrecht, Netherlands*
[65]*Institute for Nuclear Research, Academy of Sciences, Moscow, Russia*
[66]*Institute of Experimental Physics, Slovak Academy of Sciences, Košice, Slovakia*
[67]*Institute of Physics, Homi Bhabha National Institute, Bhubaneswar, India*
[68]*Institute of Physics of the Czech Academy of Sciences, Prague, Czech Republic*
[69]*Institute of Space Science (ISS), Bucharest, Romania*
[70]*Institut für Kernphysik, Johann Wolfgang Goethe-Universität Frankfurt, Frankfurt, Germany*
[71]*Instituto de Ciencias Nucleares, Universidad Nacional Autónoma de México, Mexico City, Mexico*
[72]*Instituto de Física, Universidade Federal do Rio Grande do Sul (UFRGS), Porto Alegre, Brazil*
[73]*Instituto de Física, Universidad Nacional Autónoma de México, Mexico City, Mexico*
[74]*iThemba LABS, National Research Foundation, Somerset West, South Africa*
[75]*Jeonbuk National University, Jeonju, Republic of Korea*
[76]*Johann-Wolfgang-Goethe Universität Frankfurt Institut für Informatik, Fachbereich Informatik und Mathematik, Frankfurt, Germany*
[77]*Joint Institute for Nuclear Research (JINR), Dubna, Russia*
[78]*Korea Institute of Science and Technology Information, Daejeon, Republic of Korea*
[79]*KTO Karatay University, Konya, Turkey*
[80]*Laboratoire de Physique des 2 Infinis, Irène Joliot-Curie, Orsay, France*
[81]*Laboratoire de Physique Subatomique et de Cosmologie, Université Grenoble-Alpes, CNRS-IN2P3, Grenoble, France*
[82]*Lawrence Berkeley National Laboratory, Berkeley, California, USA*
[83]*Lund University Department of Physics, Division of Particle Physics, Lund, Sweden*
[84]*Moscow Institute for Physics and Technology, Moscow, Russia*
[85]*Nagasaki Institute of Applied Science, Nagasaki, Japan*
[86]*Nara Women's University (NWU), Nara, Japan*
[87]*National and Kapodistrian University of Athens, School of Science, Department of Physics, Athens, Greece*
[88]*National Centre for Nuclear Research, Warsaw, Poland*
[89]*National Institute of Science Education and Research, Homi Bhabha National Institute, Jatni, India*
[90]*National Nuclear Research Center, Baku, Azerbaijan*
[91]*National Research Centre Kurchatov Institute, Moscow, Russia*
[92]*Niels Bohr Institute, University of Copenhagen, Copenhagen, Denmark*
[93]*Nikhef, National institute for subatomic physics, Amsterdam, Netherlands*
[94]*NRC Kurchatov Institute IHEP, Protvino, Russia*
[95]*NRC «Kurchatov»Institute - ITEP, Moscow, Russia*
[96]*NRNU Moscow Engineering Physics Institute, Moscow, Russia*
[97]*Nuclear Physics Group, STFC Daresbury Laboratory, Daresbury, United Kingdom*
[98]*Nuclear Physics Institute of the Czech Academy of Sciences, Řež u Prahy, Czech Republic*
[99]*Oak Ridge National Laboratory, Oak Ridge, Tennessee, USA*
[100]*Ohio State University, Columbus, Ohio, USA*
[101]*Petersburg Nuclear Physics Institute, Gatchina, Russia*
[102]*Physics department, Faculty of science, University of Zagreb, Zagreb, Croatia*
[103]*Physics Department, Panjab University, Chandigarh, India*

[104] *Physics Department, University of Jammu, Jammu, India*
[105] *Physics Department, University of Rajasthan, Jaipur, India*
[106] *Physikalisches Institut, Eberhard-Karls-Universität Tübingen, Tübingen, Germany*
[107] *Physikalisches Institut, Ruprecht-Karls-Universität Heidelberg, Heidelberg, Germany*
[108] *Physik Department, Technische Universität München, Munich, Germany*
[109] *Politecnico di Bari and Sezione INFN, Bari, Italy*
[110] *Research Division and ExtreMe Matter Institute EMMI, GSI Helmholtzzentrum für Schwerionenforschung GmbH, Darmstadt, Germany*
[111] *Russian Federal Nuclear Center (VNIIEF), Sarov, Russia*
[112] *Saha Institute of Nuclear Physics, Homi Bhabha National Institute, Kolkata, India*
[113] *School of Physics and Astronomy, University of Birmingham, Birmingham, United Kingdom*
[114] *Sección Física, Departamento de Ciencias, Pontificia Universidad Católica del Perú, Lima, Peru*
[115] *St. Petersburg State University, St. Petersburg, Russia*
[116] *Stefan Meyer Institut für Subatomare Physik (SMI), Vienna, Austria*
[117] *SUBATECH, IMT Atlantique, Université de Nantes, CNRS-IN2P3, Nantes, France*
[118] *Suranaree University of Technology, Nakhon Ratchasima, Thailand*
[119] *Technical University of Košice, Košice, Slovakia*
[120] *The Henryk Niewodniczanski Institute of Nuclear Physics, Polish Academy of Sciences, Cracow, Poland*
[121] *The University of Texas at Austin, Austin, Texas, USA*
[122] *Universidad Autónoma de Sinaloa, Culiacán, Mexico*
[123] *Universidade de São Paulo (USP), São Paulo, Brazil*
[124] *Universidade Estadual de Campinas (UNICAMP), Campinas, Brazil*
[125] *Universidade Federal do ABC, Santo Andre, Brazil*
[126] *University of Cape Town, Cape Town, South Africa*
[127] *University of Houston, Houston, Texas, USA*
[128] *University of Jyväskylä, Jyväskylä, Finland*
[129] *University of Kansas, Lawrence, Kansas, USA*
[130] *University of Liverpool, Liverpool, United Kingdom*
[131] *University of Science and Technology of China, Hefei, China*
[132] *University of South-Eastern Norway, Tonsberg, Norway*
[133] *University of Tennessee, Knoxville, Tennessee, USA*
[134] *University of the Witwatersrand, Johannesburg, South Africa*
[135] *University of Tokyo, Tokyo, Japan*
[136] *University of Tsukuba, Tsukuba, Japan*
[137] *Université Clermont Auvergne, CNRS/IN2P3, LPC, Clermont-Ferrand, France*
[138] *Université de Lyon, CNRS/IN2P3, Institut de Physique des 2 Infinis de Lyon, Lyon, France*
[139] *Université de Strasbourg, CNRS, IPHC UMR 7178, F-67000 Strasbourg, France, Strasbourg, France*
[140] *Université Paris-Saclay Centre d'Etudes de Saclay (CEA), IRFU, Département de Physique Nucléaire (DPhN), Saclay, France*
[141] *Università degli Studi di Foggia, Foggia, Italy*
[142] *Università di Brescia, Brescia, Italy*
[143] *Variable Energy Cyclotron Centre, Homi Bhabha National Institute, Kolkata, India*
[144] *Warsaw University of Technology, Warsaw, Poland*
[145] *Wayne State University, Detroit, Michigan, USA*
[146] *Westfälische Wilhelms-Universität Münster, Institut für Kernphysik, Münster, Germany*
[147] *Wigner Research Centre for Physics, Budapest, Hungary*
[148] *Yale University, New Haven, Connecticut, USA*
[149] *Yonsei University, Seoul, Republic of Korea*

[a] Also at: Italian National Agency for New Technologies, Energy ans Sustainable Economic Development (ENEA), Bologna, Italy.
[b] Deceased.
[c] Also at: Dipartimento DET del Politecnico di Torino, Turin, Italy.
[d] Also at: M.V. Lomonosov Moscow State University, D.V. Skobeltsyn Institute of Nuclear, Physics, Moscow, Russia.
[e] Also at: Institute of Theoretical Physics, University of Wroclaw, Poland.